PHYSICAL REVIEW B **86**, 075407 (2012)

Multiscale approach for simulations of Kelvin probe force microscopy with atomic resolution

Ali Sadeghi, Alexis Baratoff, S. Alireza Ghasemi, Stefan Goedecker, Thilo Glatzel, Shigeki Kawai, and Ernst Meyer
Department of Physics, University of Basel, Klingelbergstrasse 82, CH-4056 Basel, Switzerland
(Received 23 March 2012; revised manuscript received 21 June 2012; published 2 August 2012)

The distance dependence and atomic-scale contrast recently observed in nominal contact potential difference (CPD) signals simultaneously recorded by Kelvin probe force microscopy (KPFM) using noncontact atomic force microscopy (NCAFM) on defect-free surfaces of insulating as well as semiconducting samples have stimulated theoretical attempts to explain such effects. Especially in the case of insulators, it is not quite clear how the applied bias voltage affects electrostatic forces acting on the atomic scale. We attack this problem in two steps. First, the electrostatics of the macroscopic tip-cantilever-sample system is treated by a finite-difference method on an adjustable nonuniform mesh. Then the resulting electric field under the tip apex is inserted into a series of atomistic wavelet-based density functional theory (DFT) calculations. Results are shown for a realistic neutral but reactive silicon nanoscale tip interacting with a NaCl(001) sample. Bias-dependent forces and resulting atomic displacements are computed to within an unprecedented accuracy. Theoretical expressions for amplitude modulation (AM) and frequency modulation (FM) KPFM signals and for the corresponding local contact potential differences (LCPD) are obtained by combining the macroscopic and atomistic contributions to the electrostatic force component generated at the voltage modulation frequency, and evaluated for several tip oscillation amplitudes A up to 10 nm. For $A = 0.1$ Å, the computed LCPD contrast is proportional to the slope of the atomistic force versus bias in the AM mode and to its derivative with respect to the tip-sample separation in the FM mode. Being essentially constant over a few volts, this slope is the basic quantity that determines variations of the atomic-scale LCPD contrast. Already above $A = 1$ Å, the LCPD contrasts in both modes exhibit almost the same spatial dependence as the slope. In the AM mode, this contrast is approximately proportional to $A^{-1/2}$, but remains much weaker than the contrast in the FM mode, which drops somewhat faster as A is increased. These trends are a consequence of the macroscopic contributions to the KPFM signal, which are stronger in the AM-mode and especially important if the sample is an insulator even at subnanometer separations where atomic-scale contrast appears.

DOI: 10.1103/PhysRevB.86.075407 PACS number(s): 68.37.Ps, 07.79.Lh, 02.70.Bf, 31.15.A−

I. INTRODUCTION

Kelvin probe force microscopy (KPFM), which was introduced twenty years ago,[1,2] has become an attractive noncontact technique to determine the electric surface characteristics of materials. Among many applications, this technique has been successfully applied for mapping local work function or surface potential variations along inhomogeneous surfaces of various materials.[3–5] For a conducting crystal, the work function corresponds to the energy difference between the vacuum level outside the surface at a distance large compared to the lattice spacing, yet small compared to the lateral dimensions of a homogeneous patch, and the bulk Fermi level. In this range, which is typical for conventional KPFM measurements, the potential acting on an electron outside the surface approaches the local vacuum level and becomes constant, except in the vicinity of surface steps or patch boundaries. Differences between local vacuum levels are solely due to electrostatic contributions, which give rise to fringing electric fields around such boundaries.[6,7] If the sample is covered by a thin overlayer of foreign material, the work function can change owing to electron transfer and structural relaxation at the interface.[8] Similar changes can occur at the surface of a doped semiconductor, owing to band bending in a subsurface depletion layer. As long as electrochemical equilibrium occurs the Fermi level is aligned throughout the sample and with the Fermi level of the back electrode. However, if the sample is a wide band gap insulator, e.g., an alkali halide crystal, this equilibration may require very long times, so that the bulk Fermi level is not well defined. Charge rearrangements and relaxation occur at the interface with the back electrode and cause an additive shift of the local vacuum level outside the surface with respect to the Fermi level of the back electrode. In a real, thick enough insulator with charged impurities, such a shift will also be affected by the distribution of spatially separated charged defects at the interface, the surface and in the bulk of the sample as well as by their slow diffusion over time.[4,9]

When two separated conducting bodies, e.g., the probe tip of an atomic force microscope (AFM) and the sample, with different work functions ϕ_t and ϕ_s are connected via back electrodes, electrons are transferred until the Fermi levels become aligned. The charged bodies then develop a contact potential difference (CPD), of $V_{\mathrm{CPD}} = (\phi_t - \phi_s)/e$, where e is the elementary charge and the sample is grounded. If the tip is biased at V_b with respect to the sample, a finite electric field $\mathbf{E} \propto V$ develops in the gap between them and causes an attractive electrostatic force proportional to V^2 where $V = V_b - V_{\mathrm{CPD}}$ is their effective potential difference. If the sample is an insulator the same phenomenon occurs, but ϕ_s must be referred to the Fermi level of the back-electrode and is therefore affected by all the above-mentioned shifts, and so is V_{CPD}. It is then more appropriate to focus attention on variations of V_{CPD} along the surface rather than on its absolute value, which is affected by sample preparation.

In KPFM, a signal determined by this electrostatic force is compensated by applying a DC bias $V_b = V_{\mathrm{CPD}}$. For fast measurements, the applied bias consists of an ac modulation voltage with angular frequency $\omega = 2\pi f$ in addition to the dc voltage:

$$V_b(t) = V_{\mathrm{dc}} + V_{\mathrm{ac}} \cos \omega t. \tag{1}$$

Assuming that the electric response is linear and in-phase with V_{ac}, the electrostatic force acting on the tip can be decomposed into three spectral components:

$$F(t) = F_{\mathrm{dc}} + F_{\omega} \cos \omega t + F_{2\omega} \cos 2\omega t. \tag{2}$$

The ω component of the KPFM signal, which is proportional to $(V_{\mathrm{dc}} - V_{\mathrm{CPD}})\, V_{\mathrm{ac}}$, is selectively detected by a lock-in amplifier and compensated by a feedback circuit.

CPD variations along a surface can be conveniently measured together with its topography,[2] as determined by noncontact atomic force microscopy (NCAFM). In most state-of-the-art NCAFM experiments a microfabricated cantilever with a tip at its free end (typically etched out of doped single-crystal silicon) oscillates with a constant amplitude A at the frequency f_1 of a flexural resonance (usually the fundamental mode).[10,11] Distance-dependent tip-sample forces cause a frequency shift Δf_1 which can be very accurately measured using FM detection (frequency demodulation)[12] and used for distance control. In combined NCAFM-KPFM, the F_ω component is simultaneously sensed; either the modulated deflection signal [amplitude modulation (AM)-KPFM[13]] or the modulation of the resonance frequency shift Δf_1 [frequency modulation (FM)-KPFM[14]] is actually detected.[15,16] In either case the amplitude of the signal at the modulation frequency f is proportional to $(V_{\mathrm{dc}} - V_{\mathrm{CPD}})V_{\mathrm{ac}}$. Thus V_{CPD} can be recorded by continuously adjusting V_{dc} so that the modulation signal vanishes while scanning the tip parallel to the sample surface at a distance controlled by the (nonmodulated) shift Δf_1.[11] Both modulation techniques are much faster and more sensitive than the direct method in which V_{CPD} is determined from the extremum of the parabolic $\Delta f_1(V_b)$ curve measured by slowly sweeping V_b at each measurement point.[17–20] Potential artifacts of the modulation techniques[21] are avoided in the direct quasistatic method. Because the scope of this article is primarily theoretical, we don't further consider such experimental difficulties, but focus our attention on still controversial atomic-scale variations of the so-called local CPD (V_{LCPD}) on large, flat, overall neutral, defect-free surface areas of crystalline samples. Thus we only briefly discuss local changes due to charged surface defects[4,19,22,23] or adsorbates,[20,24] which have recently attracted considerable attention, also in theory.[25–28]

Atomic-scale variations of Δf_1 can be detected by NCAFM on well prepared surfaces in ultrahigh vacuum if the closest approach distance of the tip is smaller than the lattice spacing or the spacing between protruding atoms.[10] The contrast in Δf_1 then arises from short-range interatomic forces which begin to act in that distance range, while cantilever jump-to-contact is avoided if the total force remains much smaller than the maximum restoring force kA, k and A being, respectively, the flexural lever stiffness and oscillation amplitude.[11] Combined NCAFM-KPFM experiments have proven that FM-KPFM,[18,29–32] as well as AM-KPFM[33–35] could detect lateral atomic-scale variations of V_{LCPD} in the range where Δf_1 exhibits similar variations on surfaces of semiconductors, as well as of ionic crystals. Understanding the connections between the observed contrast in V_{LCPD} and the atomic-scale variations of the electrostatic potential just outside the surface has been a challenging task, especially on unreconstructed cleavage faces of rocksalt-type crystals.[34] Above a flat homogeneous surface V_{LCPD} must, in principle, approach the corresponding V_{CPD} at somewhat larger tip-sample separations. In practice, however, this ideal behavior is often masked by a slow dependence caused by the finite lateral resolution of surface inhomogeneities, e.g., islands of materials with different work functions. This effect is less pronounced in FM- than in AM-KPFM.[15,32,36,37] Several researchers developed models and computational schemes based on classical electrostatics which treated the tip and the sample (sometimes also the cantilever) as macroscopic bodies in order to interpret the resolution of KPFM images of inhomogeneous surfaces on lateral scales of several nanometers and above.[38–46] On the other hand, only few authors considered atomistic nanoscale tip-sample systems, either neglecting[18,26] or including the macroscopic contributions via simple approximations. In the first theoretical study of combined NCAFM-KPFM on an ionic crystal sample,[5,34,47] a formally correct partitioning was proposed between capacitive and short-range electrostatic forces induced by the effective macroscopic bias V. This analytic treatment also provided qualitative insights into the origin of atomic-scale LCPD contrast, although underestimating the capacitive force caused a quantitative disagreement with experimental results as explained in Sec. III A. More reliable results were obtained for a NaCl(001) sample interacting with a model tip consisting of a conducting sphere terminated by a small charged NaCl cluster by allowing local atomic deformations.[48] These atomistic simulations were based on the SCIFI code,[49] which has provided detailed insights into NCAFM on ionic compounds.[50,51]

In the present work, which is based on separate classical electrostatics and *ab initio* calculations, we propose a more rigorous and accurate approach for coupling interactions acting on widely different length scales schematically illustrated in Fig. 1. The macroscopic system treated by classical

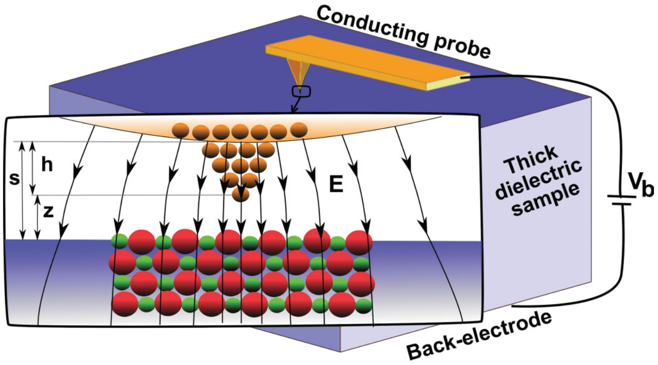

FIG. 1. (Color online) Sketch of the AFM setup showing its macroscopic and microscopic parts on two very different scales. The macroscopic tip-sample separation is $s = z + h$, where h is the nanotip height and z is the nominal distance (without relaxation) between the apex atom and the sample surface. The macroscopic electric field $\mathbf{E}$ depicted by the black field lines is applied as an external field to the atomistic subsystem shown in the zoom window.

electrostatics consists of the probe (cantilever plus tip) and of a sample described by its bulk dielectric constant. The bias voltage V_b is applied between the probe and the grounded back electrode, considered as perfect conductors. The microscopic system consists of a protruding nanotip less than 1 nm away from a slab of a few sample layers, both treated atomistically [by density functional theory (DFT) in our case]. Applying the electric field generated between the macroscopic tip and sample rather than V_b to the microscopic system leads to an unambiguous definition of V_{LCPD} on defect free, overall neutral surfaces of crystalline materials. Corrections that may be significant if the nanotip is too small or in the presence of localized charges or strongly polar species are described at the end of Secs. III A and III B. The outline of this paper is as follows: in Sec. II, we discuss previous approaches, then present our own computationally simple, yet flexible finite-difference (FD) scheme with controlled accuracy to treat electrostatic tip-sample interactions on macroscopic and mesoscopic scales. Owing to electric field penetration into the dielectric sample, the tip shank and the cantilever significantly affect the capacitive force and its gradient even at subnanometer tip-surface separations where atomic-scale contrast appears. We also explain how the influence of the effective bias V can be included into atomistic calculations, as well as shortcomings of previous attempts to do so. In Sec. III, we critically discuss previous atomistic calculations, as well as experimental evidence for short-range electrostatic interactions. Density functional calculations for nanoscale tip-sample systems are then discussed and illustrated for a realistic Si tip close to a NaCl(001) slab as an example of current interest. One important result is that the microscopic short-range force is proportional to V over a few volts; the corresponding slope is thus the basic quantity that should be extracted from KPFM measurements. In Sec. IV, expressions for V_{LCPD} in AM- and FM-KPFM are obtained and evaluated, first for ultrasmall, then for finite tip oscillation amplitude A. Their magnitude and dependence on A are explained in detail in terms of the above-mentioned macroscopic contributions to the capacitive force. Experimental limitations and evidence for the predicted trends, as well as desirable measurements are also briefly discussed. Finally, in Sec. V, the main features of our approach and of our results are summarized, and conclusions are drawn, both specific ones for our example as well as more general ones.

II. MACROSCOPIC ELECTROSTATIC INTERACTION

A. Previous approaches

Calculating the cantilever-tip-sample electrostatic interaction is, in fact, an intricate electrostatic boundary-value problem. One difficulty is due to the distance-dependent redistribution of the surface charge density on an electrode at constant bias voltage. A classical electrostatics treatment of a general system consisting of an arbitrary arrangement of conducting electrodes in the presence of a distribution of point charges in between is worked out in Ref. 52. There, the influence of the external batteries that maintain the electrodes at constant potentials as well as the polarization of the conducting electrodes by the charges are determined self-consistently. For the model macroscopic system of a semi-infinite sample and spherical tip, both treated as perfect conductors, exact expressions for the interaction energy and forces due to the bias and to polarization of the electrodes by external point charges were obtained by the analytic method of images and implemented in the SCIFI code.[49] For more realistic geometries including tip and cantilever considered in this section, even without extrinsic charges, the problem is still nontrivial. The main difficulty is due to the presence of several length scales determined by the nontrivial shape of the AFM probe. For a conducting tip represented as a cone with a spherical end cap above a conducting plane, a simple assumption (constant electric field along each field line approximated by a circular arc normal to the surfaces) led to an analytic expression for the force on the tip.[53] Recent numerical calculations[25,54] showed that Hudlet's expression is surprisingly accurate. Somewhat different analytical expressions and estimates for the lateral resolution in AM- and FM-KPFM were obtained for similar probes, also including a tilted cantilever.[41] For cylindrical geometries, many authors proposed numerical schemes based on the image charge method which is applicable to simple geometries involving spherical and planar surfaces.[55] Thus Belaidi *et al*.[56] placed N point charges on the symmetry axis and determined their positions and strengths by forcing the potential on the tip surface to be V by a nonlinear least squares fit. The previously mentioned authors also described how contributions of the spherical cap, the tip shank and the cantilever to the macroscopic force lead to characteristic distance dependencies on scales determined by the geometry and dimensions of those parts. A linearized version of the numerical image charge method where the positions of axial point and line charges were fixed was applied to study tip-shape effects for conductive and dielectric samples[42,57] and thin films on conducting substrates,[58] also including the influence of the cantilever.[59] It is not known to what extent the boundary conditions must be satisfied for a given accuracy in the numerical image method, unlike in the analytic method where the positions and strengths of the image charges change with tip-sample separation and the boundary conditions are fully satisfied (see Appendix B).

A more systematic approach to multi-length-scale problems is the boundary element method (BEM)[43,44,54]. In this method, the 3D (2D) differential Poisson's equation is transformed into 2D (1D) integral (Green's functions) equations on the surfaces of conductive or dielectric components, including CPD discontinuities and surface charges if desired.[45] The accuracy of BEM is controlled by the mesh resolution and is applicable to complex probe-sample systems, e.g., including a realistic cantilever.[60] The size of the resulting linear system of equations is small compared to volumetric discretization methods. However, because of the memory requirement of $\mathcal{O}(N^2)$ to store the fully populated matrix and complexity of $\mathcal{O}(N^3)$ to solve the linear equations, BEM has mostly been applied to systems with a relatively small number N of grid points, e.g., problems of high symmetry and homogeneity for which it is feasible to derive the Green's function analytically. Somewhat earlier a few authors adapted Green's function methods developed for more complex near-field optics problems to investigate lateral resolution in KPFM on inhomogeneous samples.[39,42] One advantage of BEM is that the LCPD of such samples can be expressed as a 2D convolution of the CPD and/or of a fixed surface charge distribution with a point-spread function which depends only on the relative position of the scanning probe.[43,54,60] The distance-dependent lateral resolution can be quantified by the width of that function. Moreover, if one assumes that only one of those distribution is present, its can be determined by inversion of the BEM matrix upon discretization on the adjustable BEM mesh.[45]

Conceptually more straightforward approaches involving surface elements have been applied to conductive probe and sample systems. In the simplest one, the tip surface is approximated as a regular staircase (or, equivalently, as an array of capacitors in parallel).[15,39,61] More accurate methods rely on adjustable meshes. Thus the finite element method (FEM) was used to calculate the electrostatic force acting on a conical tip,[40] while a commercial FEM software was recently applied to simulate a realistic cantilever and tip of actual shape and dimensions over a conducting flat sample with a CPD discontinuity.[62] More sophisticated software packages have been used to solve the Poisson's equation in the presence of space charges, e.g., for structured samples involving doped semiconductors.[38,63] Numerical methods that involve 3D discretization require a very large number of grid points even if the mesh is carefully adjusted; the computational box must therefore be truncated at some finite extent.

B. Implementation of finite-difference method

As an alternative we present a finite-difference method (FDM) on a 3D nonuniform grid which is capable of dealing with realistic sizes of the cantilever, tip, and sample. Inhomogeneous metallic and dielectric samples as well as thin dielectric films on metal substrates, can be straightforwardly treated with this method. The most attractive feature of our FDM compared to FEM or BEM computations is its ease of implementation. Since the electrostatic potential varies smoothly and slowly at distances far from the tip apex, we use a grid spacing which increases exponentially away from this region. Consequently, the number of grid points depends logarithmically on the truncation lengths, and an extension of the computational box costs relatively few additional grid points. It allows us to simulate the cantilever as well as thick dielectric samples according to their actual sizes in experiments.

The capacitance $C(s)$ between the probe and the sample back-electrode depends only on the tip-sample separation s, provided that their geometries are fixed.[64] The macroscopic electrostatic energy due to the effective voltage difference $V = V_b - V_{\mathrm{CPD}}$ between the conducting tip and back-electrode is given by $U_c(s,V) = \frac{1}{2}C(s)V^2$. The electrostatic force exerted on the tip is proportional to the capacitance-gradient $C'(s) = \partial C/\partial s < 0$,

$$F_M(s,V) = -\frac{\partial U}{\partial s} = +\left(\frac{\partial U_c}{\partial s}\right)_V = +\frac{1}{2}C'(s)V^2 < 0. \quad (3)$$

Similarly, the force-gradient is proportional to $C''(s) = \partial^2 C/\partial s^2$. We emphasize the difference between the total electrostatic energy U of the macroscopic system and the capacitive energy U_c which leads to the positive sign on the RHS of Eq. (3); the reason is restated for convenience in Appendix A. The electrostatic energy

$$U_c(s,V) = \frac{1}{2}\int \epsilon(\mathbf{r})|\nabla\Phi|^2\, d\mathbf{r}$$

can be determined once the electrostatic potential $\Phi(\mathbf{r};s,V)$ is known at any point $\mathbf{r}$ in space. In general, when the dielectric constant $\epsilon(\mathbf{r})$ varies in space, Φ satisfies the generalized form of Poisson's equation:

$$\nabla\cdot[\epsilon(\mathbf{r})\nabla\Phi(\mathbf{r})] = -\rho(\mathbf{r}), \quad (4)$$

ρ being the charge density. Minimization of the energy-like functional

$$I\,[\Psi(\mathbf{r})] = \frac{1}{2}\int \epsilon(\mathbf{r})\,|\nabla\Psi|^2\, d\mathbf{r} - \int \rho\Psi d\mathbf{r}. \quad (5)$$

subject to Dirichlet boundary conditions leads to Φ, the solution of the Poisson's equation Eq. (4) with the same boundary conditions.[55] Using a discretized variational approach, we therefore minimize the functional

$$I\,(\{\Psi_{\mathbf{n}}\}) = \sum_{\mathbf{n}}\left(\frac{1}{2}\epsilon_{\mathbf{n}}\,|\nabla\Psi|^2_{\mathbf{n}} - \rho_{\mathbf{n}}\Psi_{\mathbf{n}}\right)\upsilon_{\mathbf{n}}. \quad (6)$$

On a nonuniform grid, we delimit the volume $\upsilon_{\mathbf{n}}$ of the volume element assigned to node $\mathbf{n}$ by neighboring nodes. Then, $\Psi_{\mathbf{n}}$, $\rho_{\mathbf{n}}$, $\epsilon_{\mathbf{n}}$, and the electric field $-\nabla\Psi_{\mathbf{n}}$ are evaluated at the center of the volume element by linear interpolation between the nodes adjacent to $\mathbf{n}$ in orthogonal directions. This ensures that the field is effectively evaluated to second order in the product of grid spacings and that discontinuities in $\nabla\Psi_{\mathbf{n}}$ and $\epsilon_{\mathbf{n}}$ at material interfaces are correctly treated. Although the formalism is general and can be applied to any 3D system on a judiciously chosen nonuniform 3D orthogonal grid, in the following examples, we consider a cylindrically symmetric setup without free charges in order to allow comparison with most previous computations. In cylindrical coordinates, each volume element is a truncated tube of height $h_k^{(z)}$ with inner and outer radii r_i, r_{i+1}, respectively, and $\upsilon_{\mathbf{n}} = \pi(r_{i+1}+r_i)h_i^{(r)}h_k^{(z)}$, $h_i^{(r)} = r_{i+1} - r_i$ and $h_k^{(z)} = z_{k+1} - z_k$ being respectively the radial and vertical spacings of the appropriate nonuniform grid. The radial and vertical components of $\nabla\Psi$ are approximated on the circle of radius $r_i + 0.5h_i^{(r)}$ at $z_k + 0.5h_k^{(z)}$ as $(\Psi_{i+1,k} - \Psi_{i,k})/h_i^{(r)}$ and $(\Psi_{i,k+1} - \Psi_{i,k})/h_k^{(z)}$. Since the FD approximation of the electric field is a linear combination of the potential values on nearest-neighbor nodes, the functional in Eq. (6) is quadratic and the minimization condition $\partial I/\partial\Psi_{\mathbf{n}} = 0$ yields a system of linear equations $A\Phi = \mathbf{b}$ where the vector $\mathbf{b}$ describes imposed boundary values and charge distributions. Because $A_{\mathbf{mn}} = \partial^2 I/\partial\Psi_{\mathbf{m}}\partial\Psi_{\mathbf{n}}$ is a sparse symmetric band matrix, the system can be solved efficiently by an iterative procedure, which may, however, suffer from conditioning problems due to the nonuniformity of the grid. For an accurate solution, a mesh with high enough resolution is required in regions where $\Phi(\mathbf{r};s,V)$ varies strongly. We used the PARDISO package[65,66] to solve the resulting huge system of equations. An implementation of our FDM is distributed under GNU-GPL license as the CAPSOL code.[67]

Once $\Phi(\mathbf{r},s,V=1)$ is determined for several separations s, the system capacitance is obtained as $C(s) =$

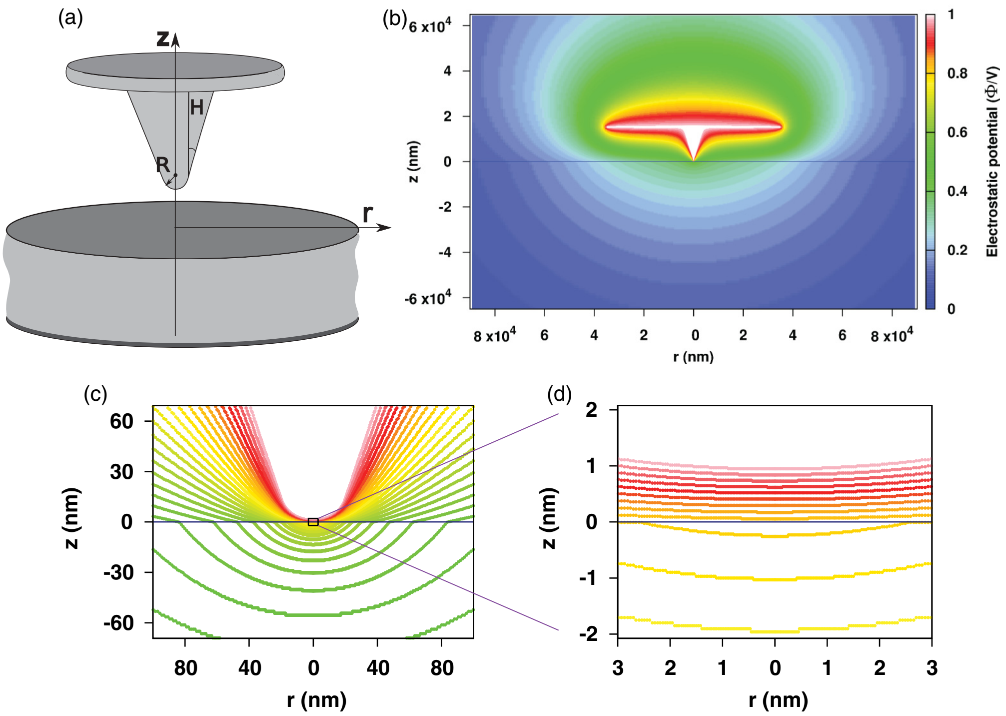

FIG. 2. (Color online) (a) Schematic of the macroscopic model AFM probe-sample system with cylindrical symmetry: a 15-nm-high cone with 15° half-angle terminated by a spherical cap of radius $R = 20$ nm is attached to a disk of thickness 0.5 μm. The radius of the disk is 35 μm that matches the area of a typical cantilever. The sample is a 1-mm-thick dielectric slab with the relative permittivity $\epsilon/\epsilon_0 = 5.9$ of NaCl. An effective bias of $V = 1$ V is applied to the conducting probe while the back electrode at the bottom and the surrounding enclosure of height and radius $10^6 R = 20$ mm (not shown) are grounded. (b) 2D (r,z) map of the macroscopic electrostatic potential Φ normalized to V for the model system in (a). The white region corresponding to $\Phi = 1$ reflects the probe geometry; successive contours differ by 0.01. The sample-vacuum interface is indicated by the horizontal line at $z = 0$ and the tip-sample separation is 1 nm. (c) and (d) Zooms into the apex-surface proximity region in (b) with 1×10^3 and 3×10^4 magnifications, respectively. The staircase shape of the contours reveals the resolution of the nonuniform mesh at different locations.

$\int \epsilon(\mathbf{r})|\nabla\Phi|^2\, d\mathbf{r} \simeq \sum_{\mathbf{n}} \epsilon_{\mathbf{n}}\, |\nabla\Phi|^2_{\mathbf{n}}\, v_{\mathbf{n}}$. Then a simple second-order FD approximation is used to evaluate $C'(s)$ and $C''(s)$ from $C(s)$. The electrostatic force acting on an arbitrary area S of a conducting part can also be evaluated as

$$\mathbf{F}_S = \frac{1}{2\epsilon_0} \int_S \sigma(s)^2 \hat{n}\, dS, \tag{7}$$

where $\sigma(s) = -\epsilon\partial\Phi/\partial n$ is the surface charge density guaranteeing that the tip surface is an equipotential, and $\hat{n}$ is the unit vector normal to the surface element dS. For a system with cylindrical symmetry, the net force on a part of the probe delimited by two cylinders of radii $r_1 < r_2$ is vertical and given by $F = \pi\epsilon_0 \int_{r_1}^{r_2} |\nabla\Phi|^2 r\, dr$, however, we prefer to use Eq. (3) to calculate the total macrosocopic force on the probe. In the following sections we validate the performance of our FDM by comparisons with previous results obtained by other methods for cylindrically symmetric systems. We mainly consider the macroscopic model system, which is shown schematically in Fig. 2(a), and is described in the caption. The conducting probe consists of a conical tip terminated by a spherical cap of radius R attached to a cantilever modeled as a disk of the same area as a typical cantilever,[39] and the sample by a thick dielectric slab. Dirichlet boundary conditions are applied on a very large cylindrical box. Figures 2(b)–2(d) show a typical computed 2D (r,z) map of the electrostatic potential normalized to effective potential V at three magnifications. Note that the grid spacing changes by six orders of magnitude (hundredths of nanometer around the tip apex to tens of μm near the box walls). The indented contours reveal the resolution of the grid at different locations, e.g., $R/400 = 0.05$ nm in the gap between tip and sample in this case. Figure 2(d) clearly shows that for a separation of 1 nm a large fraction of the voltage drop occurs within the thick dielectric sample. Whereas the contour spacing between the tip apex and the surface is constant to a good approximation, it gradually increases inside the dielectric, in contrast to what occurs in a parallel plate capacitor. Actually, the capacitance remains finite for an infinitely thick sample even in the (macroscopic) contact limit $s \to 0$ (see Appendix B).

C. Convergence and accuracy

1. Grid spacing

We first test our implementation for the problem of a conducting sphere of radius R separated by s from a semi-infinite dielectric surface for which an analytic solution of controllable accuracy is available (see Appendix B). Such a convergence analysis also yields the parameters needed to achieve a desired accuracy. Compared to the analytic solution of the sphere-dielectric system, the convergence with respect

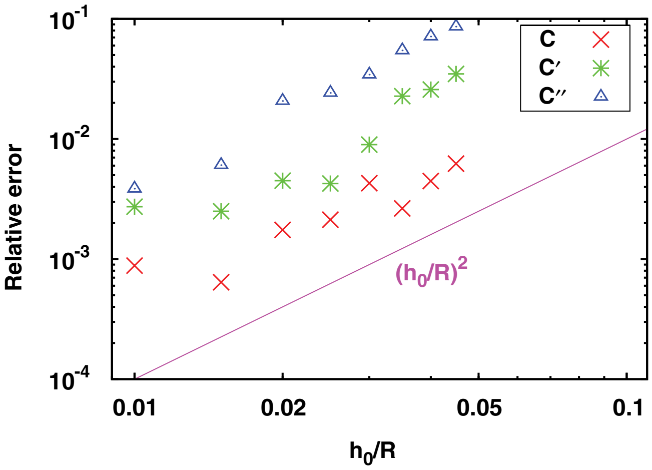

FIG. 3. (Color online) Convergence analysis with respect to the finest grid spacing h_0 for a conducting sphere of radius R in front of a thick dielectric of relative permittivity $\epsilon/\epsilon_0 = 5.9$. Points computed by our FDM for the macroscopic capacitance C, the force $\propto C'$ and force gradient $\propto C''$ are compared to the analytic solution for a semi-infinite dielectric described in Appendix B. The sphere-surface separation is $s = R/20$ and the computational box extends to $10^6 R$ in the radial and vertical directions. The straight line in the log-log plot indicates the expected quadratic error scaling (see text).

to the finest grid spacing h_0 shows a nearly quadratic error scaling (see Fig. 3) as is expected for a second-order FDM. In order to consistently preserve the shape of the tip approximated by the orthogonal mesh, the tip-sample separation must be changed in steps of h_0. Then the errors of the second-order FD approximations of C' and C'' are quadratic versus h_0, even if C is known exactly. Once these errors are added to those of C in the Poisson solver, the overall errors in C' and C'' are larger than the error in C, although they remain quadratic versus h_0, as seen in Fig. 3. The accuracy could be improved by using higher order FD approximations for the electric field by using further neighboring points. However, a corresponding improvement of the approximation of curved surfaces on the orthogonal FD mesh is then also required. Note that, for consistency, the surface of the sphere must be approximated as a staircase with variable step heights and widths which also change when the grid-spacing is changed. At larger separations, the error scaling deviates from quadratic towards linear behavior. Then the absolute value of the error is small and a larger grid-spacing can be used. The capacitance, force and force-gradient of our test system at a rather small separation of $s = R/20$ can be calculated within a relative error of 0.005 compared to the analytic solution if $h_0 = R/100$. For the cantilever-tip-sample system [see Fig. 2(a)] in the next section, a uniform grid with $h^{(r)} = h^{(z)} = h_0 = R/100$ is used around the tip apex up to a distance of twice the tip apex radius in both radial and vertical directions. Outside this range the grid becomes gradually coarser with a growth factor of 1.01.

2. *Space truncation*

A convergence analysis with respect to the size of the computational cylinder is shown in Fig. 4 for the model system described in Fig. 2. The capacitance approaches the same asymptotic value when the truncation length in a particular direction is increased while the other one is kept fixed and sufficiently large. If the computational box extends to $10^6 R$ in the radial and vertical directions, the relative deviation of the capacitance from its asymptotic value is only 10^{-7} (as indicated by the arrow in Fig. 4). We use these cutoff parameters in all subsequent FDM computations reported here.

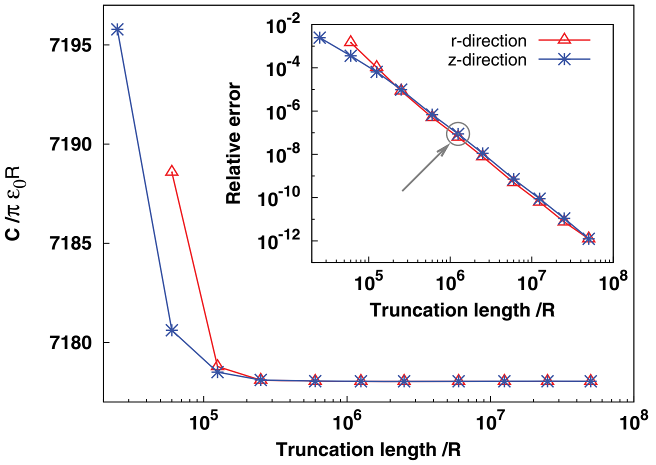

FIG. 4. (Color online) Convergence analysis with respect to the radial and vertical extents of the FDM computational box for the macroscopic system described in the caption of Fig. 2, the tip-sample separation and finest mesh size being $s = R/20$ and $h_0 = R/100$, respectively. The normalized capacitance of the system approaches the same asymptotic value upon increasing the truncation length in one direction while the other one is sufficiently large and fixed. Relative deviations with respect to the asymptotic value are shown in the inset. The arrow indicates the truncation length adopted in subsequent FDM computations.

3. *Comparison*

In Fig. 5, we compare results obtained by our FDM with previous accurate BEM computations[54] for a system like in Fig. 2(a) but without the cantilever for a conducting and a dielectric ($\epsilon/\epsilon_0 = 40$) sample. The force and the force-gradient evaluated by the two methods are in very good agreement for both kinds of samples. For the conducting sample, Hudlet's analytic approximation[53] deviates by only a few percent from the numerical results. In the following section, we show that the contribution of the cantilever can be quite appreciable for a dielectric sample.

D. Results

The macroscopic electrostatic force and force-gradient versus the normalized tip-surface separation s/R for the system in Fig. 2 are shown in Fig. 6 for three different geometries: without, with a small, and with a large cantilever modeled as disks of thickness 0.5 μm. The small disk radius is equal to the width of a typical rectangular AFM cantilever (20 μm) while the total area of the large disk (of radius 35 μm) matches the area of the rectangular cantilever. The presence of the cantilever increases the capacitance and the electrostatic force. Because the cantilever is more than 10 μm away from the surface, its contribution to the force is often

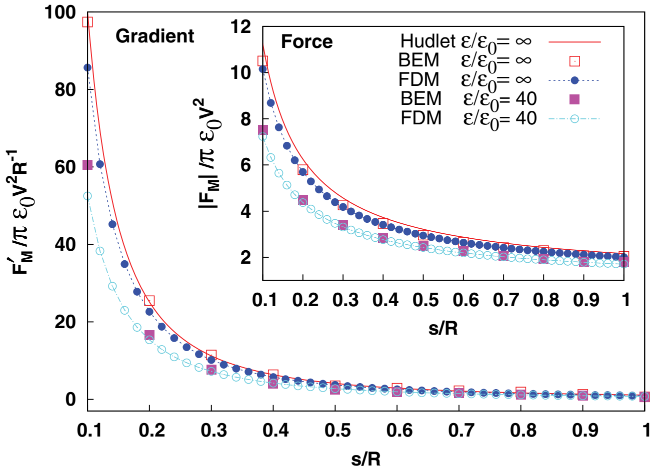

FIG. 5. (Color online) Normalized macroscopic electrostatic force (inset) and force-gradient computed by our FDM vs the normalized tip separation s/R from a dielectric ($\epsilon/\epsilon_0 = 40.0$) and a conducting ($\epsilon/\epsilon_0 = \infty$) sample compared to BEM computations (see Ref. 54) as well as to Hudlet's approximation (see Ref. 53) in the second case (see text). The cantilever is absent, as assumed in those two treatments, but the remaining parameters are as described in the caption of Fig. 2(a).

considered constant for tip-sample separations smaller than R, and therefore does not contribute to the force gradient. Our calculations [see Fig. 6(a)] confirm that this is in fact true for a conductive sample. In this case, the main contribution to the force-gradient comes from the spherical cap, as can be seen from the solid line that corresponds to the analytic solution for a conducting spherical tip (see Appendix B). However, the conical shank of the tip and the cantilever affect the force at large separations, as shown in the inset and noticed earlier.[38,39,53,56] On the other hand, if s/R is small, as shown in Fig. 6(b) and also emphasized in previous work,[57–59] over a thick dielectric sample both the force and the force-gradient are significantly decreased, owing to field penetration into the sample.

A quantity of particular relevance in our multiscale approach is the macroscopic electric field in the vacuum gap between the spherical tip end and the sample surface which polarizes the microscopic system. The variation of the electric field normalized to V/R at two points on the symmetry axis in the vacuum gap just below the tip and just above the surface versus their normalized separation is shown in Fig. 7. The same quantities, as shown magnified in the inset for nanotip separations relevant for atomic-scale contrast, i.e., $z = s - h \lesssim 0.6$ nm, differ little and drop only weakly with increasing z. In the same distance range, the z component of the electric field is two orders of magnitude stronger than the radial component parallel to the surface. These features are also clearly illustrated by the essentially equispaced horizontal equipotential contour lines in the vacuum region shown in Fig. 2(d). This important observation greatly simplifies the desired coupling to atomistic calculations: we can consider the electric field E_z at the midpoint of the macroscopic tip-surface distance $s = z + h$ as a uniform external field acting on the isolated microscopic tip-sample system. The connection between those two scales is schematically illustrated in Fig. 1.

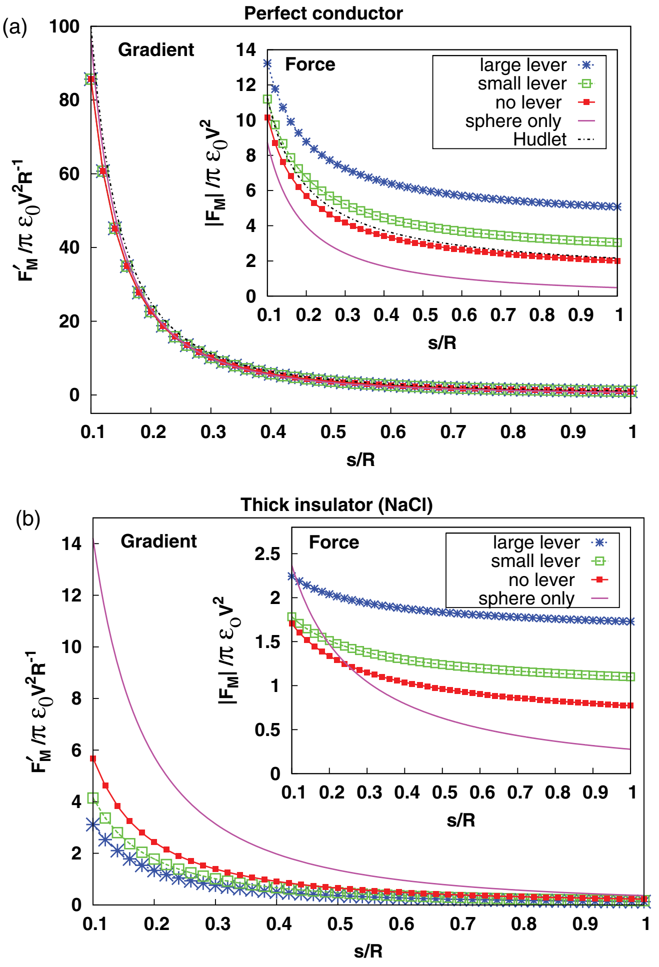

FIG. 6. (Color online) Effect of the cantilever (size) on the macroscopic electrostatic force (inset) and force-gradient at different normalized tip separations from a conducting (a) and dielectric (b) sample. The cantilever is modeled as either a small or a large disk with radii of 20 and 35 μm, respectively. Other parameters are as in caption of Fig. 2(a). The solid lines show corresponding results for a tip approximated by a conducting sphere with radius $R = 20$ nm obtained by summing the analytic series for semi-infinite samples of both kinds (see Appendix B).

Figure 6 shows that for a conducting sample the force gradient can be accurately described by a spherical tip if $s < R$, although the force itself is increasingly underestimated at larger separations.[17,53] In contrast, for a thick dielectric sample, the same description only provides the order of magnitude of F_M at small s/R, but exhibits a faster decrease with increasing separation and overestimates F'_M. Figure 7 reveals that a spherical model tip overestimates the electric field E_z under the tip at all separations, which then approaches V/R on the sphere (and zero on the surface) when $s \gg R$. This occurs because the induced surface charges can spread to the conical shank and the cantilever in the more realistic model. The contributions of those parts to the force F_M become nevertheless stronger than that of the sphere alone already at small s/R. In general, if $s/R \to 0$, the electric field under the tip, hence the force and the force gradient are enhanced owing to an increasingly localized surface polarization of both tip and sample, but remain finite if the sample is a dielectric,

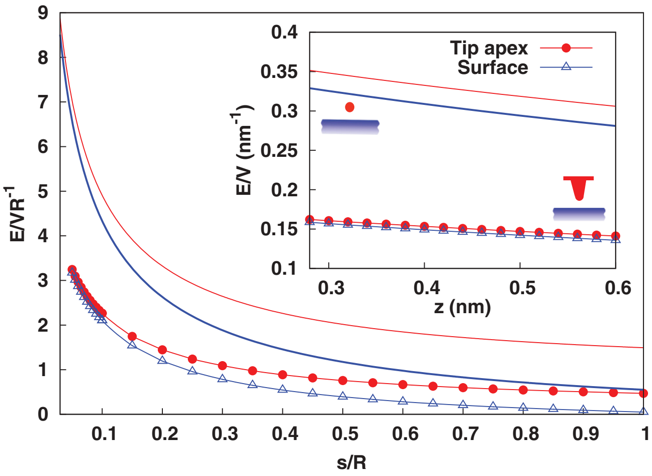

FIG. 7. (Color online) Normalized macroscopic electric field in the vacuum on the tip surface and on the dielectric sample surface ($\epsilon/\epsilon_0 = 5.9$) vs their normalized separation for the probe described in the caption of Fig. 2(a) (curves with symbols) and for a tip approximated by a conducting sphere of the same radius (continuous curves). Inset: zoom into the range $z = s - h$ where atomic-scale contrast appears for $R = 20$ nm, $h = 0.72$ nm; the electric field between the tip and the surface changes by only a few percent and is hence nearly uniform.

as explicitly demonstrated by the solution for a spherical tip (see Appendix B). Comparison with that solution (the solid curves in Fig. 6) shows that even at small separations both the conical shank and the cantilever contribute to the force, whereas mainly the conical shank affects the force gradient. Hence ignoring those contributions causes an overestimation of the force-gradient if the sample is an insulator.

III. SHORT-RANGE ELECTROSTATIC FORCES

A. Evidence and previous models

When an AFM tip approaches a surface, short-range forces contribute to the tip-sample interaction and give rise to atomic-scale contrast in NCAFM. Hereafter, F_μ denotes the short-range force component perpendicular to the surface which can be extracted from measurements of Δf_1 versus the closest tip approach distance d in an oscillation cycle.[68,69] The contrast observed in V_{LCPD} in the same distance range cannot only be due to the long-range electrostatic force, but must be due to a short-range bias-dependent force. Arai and Tomitori were the first to infer the existence of such a force from $\Delta f_1(V_b)$ curves recorded with a cleaned and sharpened silicon tip closer than 0.5 nm to a 7 × 7 reconstructed Si(111) surface.[70] In particular, above a Si adatom, they found a narrow peak growing with decreasing d superposed on the usual parabolic dependence around the plotted minimum of $-\Delta f_1(V_b)$ in their Fig. 1, i.e., for $V_b \simeq V_{\mathrm{CPD}}$. Later the same authors pointed out that an even sharper peak appeared at the same bias in the simultaneously recorded tunneling current.[71] This seemingly supported their original suggestion that the additional attractive force causing the peak in $-\Delta f_1(V_b)$ arose from the increased overlap due to the bias-induced energetic alignment of dangling bonds states localized at the tip apex and on Si surface adatoms. The formation of a covalent bond between those states has been shown to be responsible for the observed NCAFM contrast on the 7 × 7 reconstructed Si(111) surface.[72] In extensive recent measurements on the same system, however, Sadewasser *et al.* reported parabolic $\Delta f_1(V_b)$ curves, but detected a rapid drop by about -1 V followed by a gradual increase in V_{LCPD} above a Si adatom with decreasing d in the range where the extracted short-range force showed a similar behavior.[18] The apparent discrepancy with respect to Arai and Tomitori's observations is not so surprising because tunneling is seldom observed with clean silicon tips, although it is routinely measured in STM as well as in NCAFM on conducting and even semiconducting samples when using metal-coated silicon tips.[73,74] An appreciable position- and distance-dependent dc tunneling current complicates the interpretation of LCPD measurements. This problem does not arise with insulating samples, but conversion to a dc transport current below the surface of a weakly doped semiconductor can cause a significant voltage drop within the sample owing to the finite bias required to compensate the LCPD. Especially in quasistatic measurements of $\Delta f(V_b)$ away from the compensation voltage, a strong dc electrostatic "phantom" force is generated which gives rise to atomic-scale contrast in NCAFM at separations where none is expected.[75,76] Nevertheless, Arai and Tomitori's basic idea that bias-induced alignment of spatially localized surface states can lead to an enhanced site-dependent attractive force remains plausible even if a dc tunneling current cannot be sustained. Thus Krok and coworkers[32] suggested that the lower LCPD which they found across protruding In rows on the c(2 × 8) reconstructed InSb(001) surface was due to a bias-induced local electron transfer from a polar dangling bond on the electronegative Sb atom presumably picked by the Si tip to the nearest electropositive surface In atoms. The same authors also showed that the LCPD contrast between different lateral positions decays exponentially with increasing $d < 1$ nm.

The few simulations of KPFM based on DFT computations have been concerned with silicon model tips interacting with reconstructed Si surfaces, both clean and containing substitutional impurities. None of those purely microscopic calculations took into account the macroscopic capacitive contribution to the KPFM signal, however. Thus Sadewasser *et al.*[18] obtained qualitative agreement between variations of the perpendicular dipole moment and of the local chemical potential of their microscopic subsystem, both computed at zero bias, and the distance dependence of V_{LCPD} measured by FM-KPFM on the benchmark-like Si(111) 7 × 7 surface. Masago and coworkers[26] defined the V_{LCPD} within a tight-binding-based DFT formalism as the difference between the Fermi levels (electrochemical potentials) of their tip and sample microscopic subsystems, which were forced to carry opposite charges determined so as to minimize the force on their nanotip. Although overlap between tip and sample wave functions was neglected, qualitatively correct V_{LCPD} images of charged surface and subsurface defects were obtained based on Coulomb interactions between Mulliken charges treated as point objects. Very recently, the same authors included wave-function overlap to first order,[28] and generated V_{LCPD} images showing partially occupied dangling bonds on the 5 × 5 analog of the Si(111) 7 × 7 surface at a smaller distance

(0.4 nm) where a covalent bond begins to form between a dangling bond at the tip apex and a Si adatom.

Whereas bias-induced electron transfer is plausible for narrow-band-gap semiconductors like those previously mentioned, it is unlikely for overall neutral cleaved (001) surfaces of wide-band gap insulators like alkali halides that neither have gap states nor are reconstructed, but are only weakly rumpled.[77] In Ref. 34, the atomic-scale LCPD contrast observed on KBr(001) was attributed to opposite surface cation and anion displacements in response to local electric fields induced by the macroscopic (in accordance with our definition) field. However, the authors approximated E_z by the electric field V/R at the surface of an isolated conducting spherical tip, the local unit cell polarizability by the bulk crystal (Clausius-Mosotti) expression, and neglected the macroscopic surface polarization. Although essentially constant on the scale of a nanometer-size nanotip, the latter, together with E_z is actually nonuniform on a lateral scale of order $\sqrt{Rs}$ for separations $s \ll R$. They evaluated the macroscopic and microscopic surface charges densities σ_m and σ_μ induced on a conducting model tip by their E_z and by the displaced surface ions, respectively. Using Eq. (7), they computed the modulation of the electrostatic force. After further justified approximations, they obtained opposite LCPDs above cations and anions, which increased exponentially with d. In a subsequent article,[47] the same authors added a macroscopic force roughly representing the interaction of the cantilever with the back electrode, but still obtained a surprisingly large maximum in the absolute LCPD for $d \simeq 0.6$ nm. In a subsequent publication,[48] more reliable results were obtained with the SCIFI code[49] for a cubic NaCl cluster partly embedded into a conducting sphere interacting with a NaCl(001) sample similar to ours via empirical shell-model potentials. Cluster ions inside the sphere were fixed, while the protruding cluster ions formed a small nanotip with a net charge $+e$ at the apex. The protruding ions were allowed to relax and to induce image charges in the electrodes. The results obtained can be considered representative of what is expected for a small, charged nanotip interacting with an ionic crystal. A common justification for such a model is that real tips often pick up sample material and that simulations based on the same code produced reasonable results when compared to NCAFM measurements on ionic crystals, alkali halides in particular.[50,51] However, in those and in previous SCIFI computations[78,79] using a larger protruding ionic nanotip against an overall neutral defect-free sample slab, the inclusion of electrode polarization was deemed unnecessary. Indeed, contributions from images charges of close anion-cation pairs tend to cancel out if $R \gg z$. More importantly, according to the Supplemental Material of Ref. 25, the distance dependence of V_{LCPD} calculated analytically for a single charge or dipole fixed below a conducting sphere facing a biased planar counter-electrode coincides with the results of full SCIFI computations including image charges. This is observed down to a separation s of 0.7 nm for a small charged nanotip similar to that assumed in Ref. 48, whereas the much smaller V_{LCPD} obtained for the larger nanotip assumed in the above-mentioned SCIFI computations is compatible with a smaller permanent dipole moment. The coincidence implies that at larger separations the electrode polarizations induced by the charge q and by the effective bias $V = V_b - V_{\mathrm{CPD}}$ are decoupled. Coupling presumably arises at separations approaching interatomic distances where ions (or atoms) inside the microsystem become appreciably polarized (electronically and/or owing to induced displacements) by local fields,[27] thus leading to the site-dependent LCPD contrast superposed on the z-dependent long-ranged LCPD obtained in Ref. 48. In the absence of localized, pointlike net charges (or permanent dipoles) in the microsystem, the resulting force due to polarization of the microsystem and of the electrodes is proportional to V^2. It is, however, overwhelmed by the macroscopic capacitive contribution discussed in Sec. II A if the nanotip dimensions are small compared to R.

Earlier studies mentioned that the short-range tip-sample interaction is bias dependent but provided no recipe to investigate it theoretically. Moreover, they did not clarify how long-range and short-range bias-dependent forces are connected and the role of each in the observed KPFM signals. In the following sections, we answer all of these questions and obtain and analyze in detail theoretical expressions for the site-dependent LCPD. Our approach is not limited to particular materials, but results are presented for the system described in the following section, which is representative of a neutral, but polarizable reactive clean Si tip interacting with an ionic crystal.

B. Density functional computations

As illustrated in Fig. 1 our microscopic system consists of a nanotip of height h protruding from the spherical end of the macroscopic tip and of a wider two-layer slab of sample atoms. Computations are performed within the local-density approximation to density functional theory (DFT) using norm-conserving HGH pseudopotentials[80] and the BigDFT package.[81] Relying on a wavelet basis set with locally adjustable resolution, this package calculates the self-consistent electron density, the total energy and its electrostatic component with selectable boundary conditions,[82] i.e., periodic in two directions and free in the third in our case. This allows us apply an external field perpendicular to the surface without artifacts which can arise from periodic images in the z direction when using plane-wave of mixed basis sets. As already explained, the voltage biased macroscopic system determines the uniform electric field $E_z \propto V = V_b - V_{\mathrm{CPD}}$ applied to the microscopic part (see Fig. 1). This provides the desired well-defined relationship between the bias-voltage and short-range forces, which was lacking in previous approaches to LCPD contrast based on DFT computations.[18,26,28]

Figure 8 illustrates the microscopic system used in the DFT computations reported here. The nanotip at the very end of a silicon tip is modeled as a cluster with a fixed (001) base of eight Si atoms with all dangling bonds passivated by H atoms in order to mimic the connection to the rest of the tip. The remaining Si atoms were prerelaxed using the minima hopping method[83] previously employed to generate low-energy structures of silicon clusters and of similar model tips.[84] As in that work, the free Si atoms adopted a disordered configuration with several exposed under-coordinated atoms. In particular, the protruding apex atom is threefold coordinated and hence has a dangling bond with a small dipole moment pointing towards the surface. As we verified, a distance five

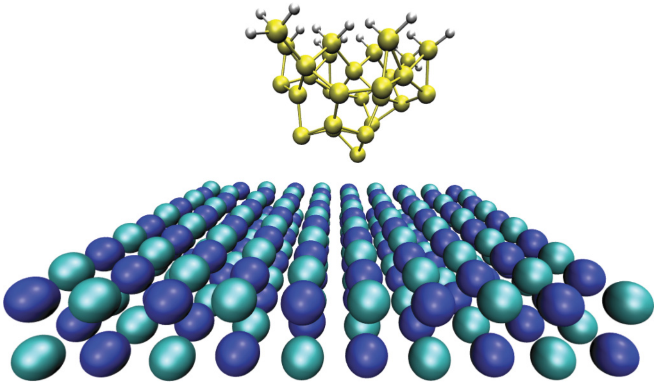

FIG. 8. (Color online) The microscopic Si-tip NaCl-slab system used in our *ab initio* DFT calculations. The apex of a silicon AFM tip is modeled as a prerelaxed $Si_{29}H_{18}$ cluster. All eight atoms in the top (001) layer are passivated by hydrogen atoms and kept fixed. The position of the foremost Si atom is (x,y,z), z being its nominal distance from the surface. The model sample consists of two NaCl(001) layers each containing 10 × 10 ions with the bottom layer kept frozen. Periodic boundary conditions are applied along the x and y directions.

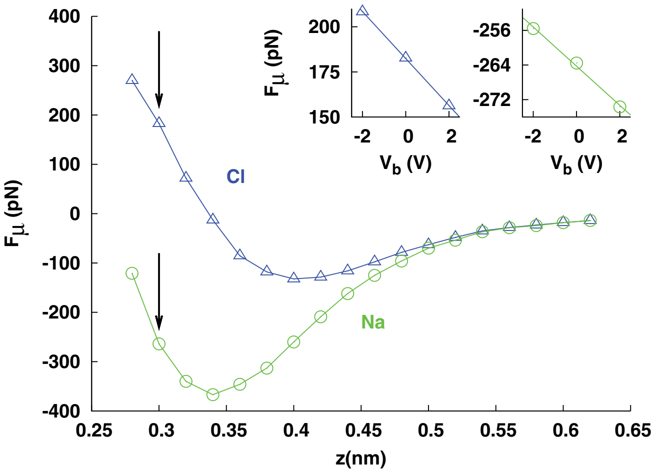

FIG. 9. (Color online) Microscopic force on the Si nanotip above Na and Cl surface ions from ab initio calculations without an applied electric field. Insets: variation of the force as a function of the macroscopic bias voltage at a tip-surface separation of 0.30 nm.

times the lattice constant of NaCl is large enough to get rid of the electrostatic interaction between this nanotip and its images in the main in-plane symmetry directions along which periodic boundary conditions applied. Therefore our sample slab consists of two 10 × 10 NaCl(001) layers containing 200 ions in total. For such a large system, it is sufficient to perform calculations only at one single k-point, namely, center of the surface Brillouin zone. Pre-relaxation of the sample only caused a small rumpling which preserved the basic periodicity of the truncated (001) surface. Although the silicon model tip and the sample were initially individually prerelaxed, all tip and sample atoms were subsequently frozen in some of our KPFM simulations. In this way, we could assess pure electronic polarization effects without effects due to the interaction-induced displacements of ion cores.

The silicon model tip was positioned so that its foremost atom was 0.65 nm above a sodium and chlorine surface ion, then moved towards the sample in steps of 0.02 nm. At each step the Kohn-Sham equations are solved iteratively. The topmost layer of the Si tip together with the passivating H atoms as well as the bottom layer of the slab are kept fixed, while other ions are free to relax until the Hellman-Feynman force exerted on each ion is less than 1 pN. This extremely tight tolerance is required only when the relative variation of the force when the bias changes is very small. The force F_μ exerted on the model tip is obtained by summing the z components of the forces over atoms of the tip. Since the free atoms are well relaxed, their contribution to that force is not significant and was used as a measure of the error in forces. Figure 9 shows the microscopic force versus the tip-apex separation from Cl and Na surface sites without applied electric field. The same procedure is repeated at each tip-sample separation for a few field strengths E_z determined as explained in Sec. II D for effective biases $-2 \leqslant V = V_b - V_{\mathrm{CPD}} \leqslant 2$ V applied to the macroscopic tip. For such biases and distances where F_μ becomes site dependent, a nearly uniform macroscopic electric field of ∼0.15 V/nm occurs in the vacuum gap, as discussed in Sec. II and illustrated in the inset of Fig. 7. No instabilities caused by electronic and/or atomic rearrangements appeared in that range of parameters. The variation of the force at the particular separation $z = 0.3$ nm is shown in the insets in Fig. 9. In contrast to the macroscopic capacitive force, the short-range force depends linearly on the applied bias voltage. As explained elsewhere,[85] this linear term is remarkably close to the interaction between distance-dependent but V-independent charge densities on the tip and sample with the macroscopic electric field. Earlier studies obtained such a term by treating native ions or charged atoms adsorbed on the sample surface and/or the tip apex as point charges.[25,27,34] Deviations from the linear behavior could occur for larger biases, especially near instabilities, as observed in computations for a charged nanotip.[48]

The basic quantity which determines the deviation of the LCPD from the background CPD is the voltage-independent slope of the short-range force with respect to the applied voltage

$$a(x,y,z) = \frac{\partial}{\partial V} F_\mu(x,y,z;\mathbf{E}(V)). \tag{8}$$

As discussed in Introduction, the background CPD is not a well defined quantity for an insulator. For a real doped silicon tip-NaCl(001) sample, it would be different from the CPD of our microscopic system if charge equilibrium is achieved, as enforced by the self-consistency of the computations. Besides, no CPD is explicitly included in the description of the macroscopic system. Thus the effective bias $V = V_b - V_{\mathrm{CPD}}$ would differ from that in a real system. Nevertheless, as long as this bias is in the Volt range, the slope a is unaffected.

Figure 10(a) shows that the slope a exhibits a characteristic site-dependent distance dependence at separations less than 0.5 nm, and is larger above the more polarizable Cl ion. The underlying physics will be explained elsewhere.[85] The microscopic force-gradient F'_μ is also a linear function of bias voltage, and the distance dependence of its slope $a'(x,y,z) = \partial F'_\mu/\partial V$, approximated to second order by linear interpolation between adjacent points on both sides of a given z value, is

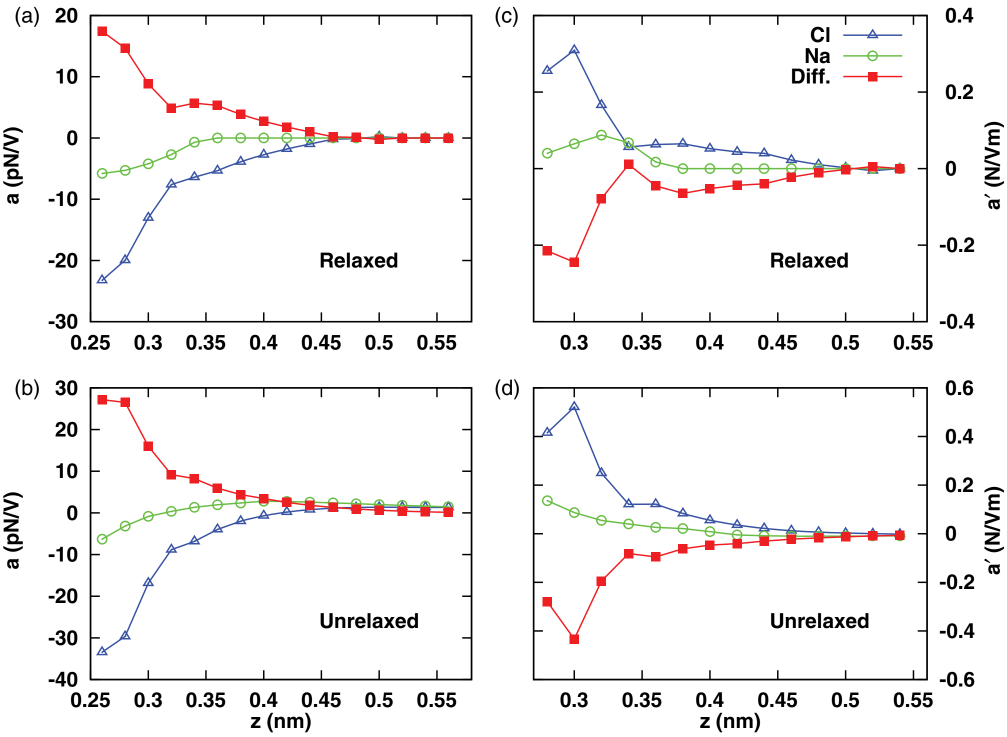

FIG. 10. (Color online) Distance-dependence of the slopes $a = \partial F_\mu/\partial V$ and $a' = \partial F'_\mu/\partial V$ above Na and Cl surface ions with [(a) and (c)] and without [(b) and (d)] relaxation of the free atoms and ions during tip approach. The difference (contrast) between Na and Cl sites is shown by red (filled) symbols.

shown in Fig. 10(c). Figures 10(b) and 10(d) show that a and a' are weaker if relaxation is allowed but that contrast appears below nearly the same distance and exhibits almost the same distance dependence. Thus, for the assumed neutral Si nanotip, the contrast is mainly due to electronic polarization rather than to bias-induced ion displacements.

In the approximation that the macro- and microscopic systems are coupled only through the macroscopic electric field, the z component of the total force exerted on the tip is

$$F = F_M(s;V) + F_\mu(x,y,z;V) + F_{\mathrm{vdW}}(s), \qquad (9)$$

where $s = z + h$ and $V = V_b - V_{\mathrm{CPD}}$. The long-range van der Waals force F_{vdW} is bias and site independent. Being only a function of the mesoscopic geometry it is therefore henceforth ignored, although it affects the resonance frequency shift Δf in a NCAFM measurement. The macroscopic force F_M is capacitive ($\propto V^2$) while the microscopic force F_μ has been shown to be linear in V.

Three additional corrections couple the bias-dependent macro- and microscopic forces. The first correction $\delta C' V^2/2$ is due to an additional capacitive contribution caused by the presence of a polarizable nanoscale object in the gap between the macroscopic bodies. Owing to the small lateral dimensions of the nanotip compared to the radius of the macroscopic tip end, this correction is small,[27,85] although it can become noticeable and site dependent if the nanotip is strongly polarizable and nearly contacts the sample.[27,48]

The second correction arises if the microsystem contains a localized net charge[49] or permanent dipole moment.[86] This leads to a site-independent LCPD with an approximate power-law approach towards a background CPD of several volts. The interaction of the nanotip charge distribution with the macroscopic field **E** could, in principle, be included in our description at separations s where **E** can no longer be considered uniform. In that range, however, the charge or dipole might be approximated as point objects, as justified in the case of a conducting sample in the Supplemetal Material of Ref. 25. Because the charge or dipole are intrinsic, the interaction is proportional to V, so that this correction would give rise to long-range contributions to the slopes a and a'.[25,27] In the case of our neutral Si nanotip and sample slab, this correction is small.

The third correction arises because in reality the nanotip is in electrical contact with the macroscopic tip, so that the electron density at the interface differs from that near the top of our isolated silicon cluster. However, this model tip is large enough, so that the charge distribution near the apex, which dominates F_μ is not much affected. The microscopic force is computed from the self-consistently determined microscopic electron density and ion core positions. The resulting electric field between the nanotip apex and the sample surface is nonuniform and differs from the original applied macroscopic field E_z.

IV. AM AND FM KPFM SIGNALS AND LOCAL CONTACT POTENTIAL DIFFERENCES

A. Ultrasmall amplitude limit

The force gradient is more sensitive than the force to short-range interactions which are responsible for atomic-scale contrast in NCAFM and KPFM. Direct detection of the gradient is in principle possible if the variation of F_μ over the peak-to-peak oscillation amplitude is linear, e.g., if $2A$ is comparable to the spacing 0.02 nm of the computed points in Fig. 9. We first consider this simple limit which is commonly assumed in the KPFM literature, but is seldom achieved in NCAFM experiments. As explained in Introduction, V_{LCPD} is operationally defined by nulling the KPFM signal generated by the force component F_ω at the modulation frequency. Assuming that the response V_{ac} is linear and instantaneous, $F_\omega = (dF/dV_b)V_{\mathrm{ac}}$, and the deflection signal detected in AM-KPFM would be proportional to

$$F_\omega = [C'(z+h)(V_{\mathrm{dc}} - V_{\mathrm{CPD}}) + a(x,y,z)]V_{\mathrm{ac}} \qquad (10)$$

in the ultrasmall amplitude limit, and would be nulled if

$$V_{\mathrm{dc}} = V_{\mathrm{CPD}} - \frac{a(x,y,z)}{C'(z+h)}. \qquad (11)$$

Because the background V_{CPD} is not well defined, and only $a(x,y,z)$ is site dependent, we consider only the deviation of V_{LCPD} from V_{CPD}, which is responsible for atomic-scale contrast, i.e.,

$$\Delta V_{\mathrm{LCPD}}^{\mathrm{AM}} = -\frac{a(x,y,z)}{C'(z+h)}. \qquad (12)$$

As illustrated by the points for $A = 0.01$ nm in Fig. 11(d), for a dielectric sample, the z-dependence of C' is weak over the range ($s = z + h < 1$ nm) where $a(x,y,z)$ is appreciable, cf. Fig. 10(a) (note that the ultrasmall amplitude $A = 0.01$ nm is equivalent to $A \to 0$ in our calculations, as discussed in the following section). Therefore ΔV_{LCPD} differs from $a(x,y,z)$ by an essentially z-independent factor. Depending on the nanotip height h, this may no longer hold in the case of a conductive sample or thin dielectric film on a conductive substrate.

In FM-KPFM, the contribution of the modulated electrostatic force component F_ω to the frequency shift of the first resonant mode Δf_1 is detected and nulled. In the ultrasmall amplitude limit, Δf_1 is proportional to the force gradient[12] and

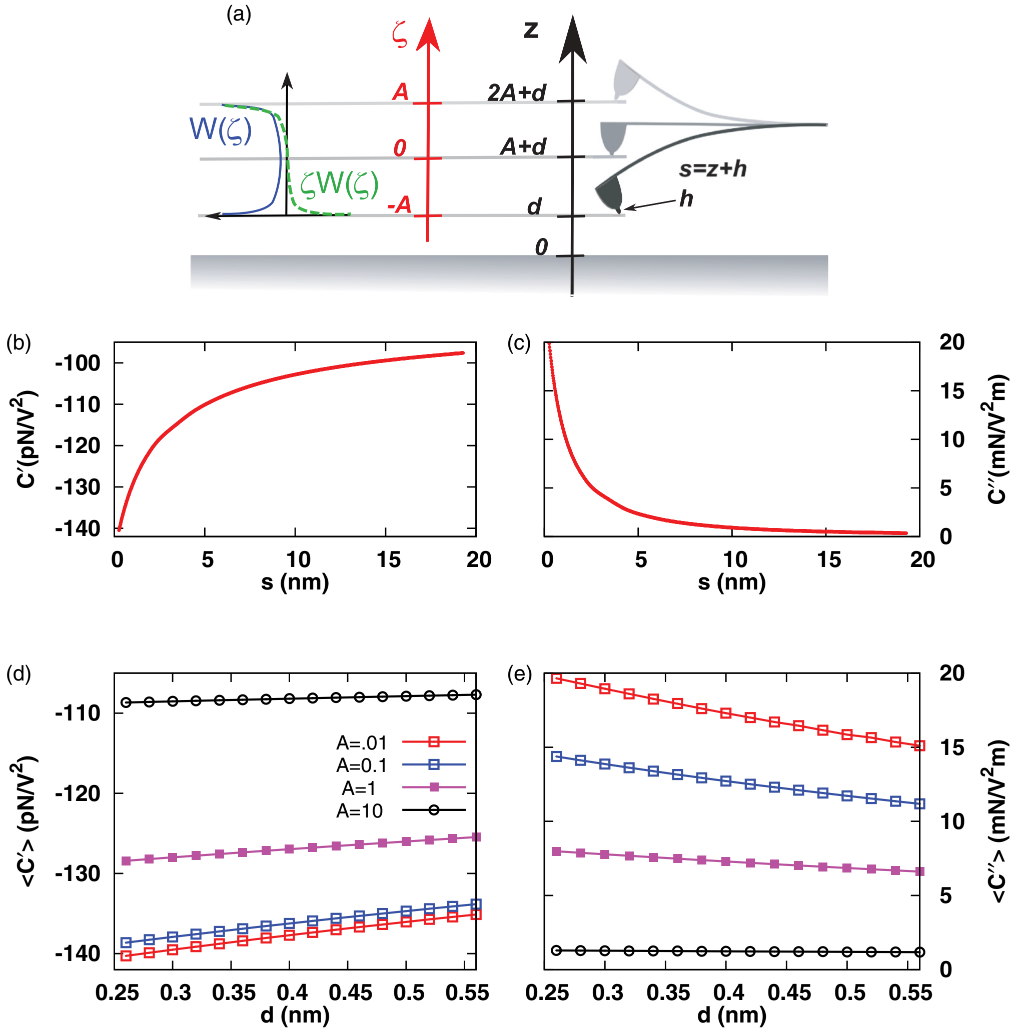

FIG. 11. (Color online) (a) Sketch of the cantilever-tip probe oscillating in its fundamental mode with a finite amplitude A; d is the closest approach distance of the nanotip apex. The weight functions used in Eqs. (16) and (17) to calculate the cycle averages are plotted as functions of $\zeta = z - d - A$. Dependencies of the first (b) and second (c) spatial derivatives of the capacitance on the macroscopic separation $s = z + h$ calculated for the setup in Fig. 2(a), and of their cycle averages (d) and (e) on d for tip oscillation amplitudes $A = 0.01$, 0.1, 1, and 10 nm.

would therefore be nulled if

$$F'_\omega = [C''(z+h)(V_{\rm dc} - V_{\rm CPD}) + a'(x,y,z)]V_{\rm ac} = 0.$$

The FM counterpart of Eq. (12) is therefore

$$\Delta V^{\rm FM}_{\rm LCPD} = -\frac{a'(x,y,z)}{C''(z+h)}. \tag{13}$$

The site and distance dependence of $\Delta V^{\rm FM}_{\rm LCPD}$ is determined by $a'(x,y,z)$ because in the range $s < 1$ nm where a' is appreciable, cf. Fig. 10(c), the denominator of Eq. (13) is almost z independent as illustrated by the points for $A = 0.01$ nm in Fig. 11(e). The calculated LCPD deviations for $A = 0.01$ nm in the AM and FM modes are plotted in Figs. 12(a) and 12(e). For the ultrasmall amplitude $A = 0.01$ nm, which would likely not provide an adequate signal-to-noise ratio in practice, the calculated $\Delta V^{\rm FM}_{\rm LCPD}$ is about hundred times stronger than $\Delta V^{\rm AM}_{\rm LCPD}$ and exceeds the range of validity (±2 V) of our DFT computations as well as the range of experimentally measured values. Therefore it is important to consider averaging over the range covered by the finite tip oscillation.

B. Finite amplitude expressions

In NCAFM with cantilevers, the oscillation amplitude A is between several and a few tens of nanometers, so that the macroscopic capacitive electrostatic force can change by several orders of magnitude over an oscillation cycle. In practice, the detected AM and FM-KPFM signals are given by differently weighted averages, namely,[35]

$$\langle F_\omega\rangle = \frac{1}{2\pi}\int_0^{2\pi} F_\omega[d + A(1+\cos\phi)]d\phi$$

and[87]

$$kA\frac{\Delta f_\omega}{f_\omega} = -\frac{1}{2\pi}\int_0^{2\pi} F_\omega[d + A(1+\cos\phi)]\cos\phi d\phi,$$

where k is the flexural stiffness of the cantilever and $d = z_{\rm min}$ is the closest tip apex-sample separation. Substituting the force from Eq. (10) and setting these averages to zero, one obtains

$$\Delta V^{\rm AM}_{\rm LCPD} = -\frac{\langle a(x,y,z)\rangle_w}{\langle C'(z+h)\rangle_w}, \tag{14}$$

$$\Delta V^{\rm FM}_{\rm LCPD} = -\frac{\langle a'(x,y,z)\rangle_{1/w}}{\langle C''(z+h)\rangle_{1/w}}, \tag{15}$$

where the cycle averages depend both on d and A and are defined as

$$\langle g\rangle_w \equiv \frac{1}{\pi}\int_{-A}^{A} w(\zeta)g(d+A+\zeta)d\zeta, \tag{16}$$

$$\begin{aligned}\langle g'\rangle_{1/w} &\equiv \frac{1}{\pi A}\int_{-A}^{A}\zeta w(\zeta)g(d+A+\zeta)d\zeta\\ &= \frac{1}{\pi A^2}\int_{-A}^{A}\frac{1}{w(\zeta)}g'(d+A+\zeta)d\zeta.\end{aligned} \tag{17}$$

As depicted in Fig. 11(a), $\zeta = z - (A+d)$, whereas the weight functions $w(\zeta) = 1/\sqrt{A^2-\zeta^2}$ and $\zeta w(\zeta)$ have square root singularities at the turning points of the oscillation. Note that if $A \to 0$ then $\langle g\rangle_w$ tends to $g(d+A)$. Similarly, the expression on the second line of Eq. (17) justifies the notation $\langle g'\rangle_{1/w}$ and shows that this quantity tends to $g'(d+A)$ when $A \to 0$, besides helping to relate the distance dependence of $\Delta V^{\rm FM}_{\rm LCPD}$ to those of $a'(x,y,z)$ and $C''(z+h)$. However, because $a(x,y,z)$ is computed with high precision, whereas $a'(x,y,z)$ is obtained by interpolation, we use the expression on the first line for numerical purposes. Furthermore, since $a(x,y,z)$ is known only at equispaced separations z_i where the DFT computations have been performed, the integrals in Eqs. (16) and (17) must be discretized. The adopted procedure, which deals with the singularities of the weight function $w(\zeta)$ at the integration limits,[88] is presented in Appendix C. There we also show that the discretized version of the expression in the first line of Eq. (17) reduces to the second-order FD approximation of $g'(d+A)$ when $2A$ matches the spacing between adjacent z_i values, in accordance with the expression on the second line.

C. Results

Owing to the very different z dependencies of $a(z)$ and $C'(z+h)$, shown respectively in Figs. 10(a) and 11(b), their cycle averages depend in different ways on d and A. The same holds for $a'(z)$ and $C''(z+h)$, shown respectively in Figs. 10(c) and 11(c). Figures 11(d) and 11(e) show the cycle averages of C' and C'' versus the closest tip-apex approach distance d for oscillation amplitudes $A = 0.01, 0.1, 1,$ and 10 nm, whereas the cycle averages of $V_{\rm LCPD}$ calculated from Eqs. (14) and (15) are plotted in Fig. 12 for AM-KPFM (left column) and FM-KPFM (right column) for the same amplitudes in the range where $a(z)$ is finite. In that range, the cycle averages for $A = 0.01$ nm agree with the nonaveraged quantities. Since the primary quantities were calculated at points spaced by 0.02 nm, this is not surprising in view of the remarks at the end of the preceding section. Thus apart from small deviations introduced by the discretization procedure, the points in Figs. 12(a) and 12(e), which were actually calculated for $A = 0.01$ nm coincide with those given by Eqs. (12) and (13), and exhibit essentially the same distance dependencies as $a(d)$ and $a'(d)$, as already discussed in Sec. IV A.

Already above $A = 0.1$ nm, however, the LCPD contrasts in both modes exhibit almost the same spatial dependence as $a(d)$, although their respective magnitudes decrease if A is increased. Nevertheless, $\Delta V^{\rm FM}_{\rm LCPD}$ significantly exceeds $\Delta V^{\rm AM}_{\rm LCPD}$; this can be understood as follows. As seen in Figs. 11(d) and 11(e), $\langle C''\rangle_{1/w}$ drops much faster than $-\langle C'\rangle_w$ if A is increased. As explained in the discussion of Fig. 6(b), this behavior reflects the increasing influence of the relative contributions of the tip shank and of the cantilever to $C'(z+h)$ in the range covered by the peak-to-peak oscillation. Especially $\langle C'\rangle_w$ is affected by the cantilever contribution which causes the very gradual levelling of $C'(z+h)$ apparent in Fig. 11(b). As seen in Fig. 11(c), this slowly varying contribution tends to cancel out in $C''(z+h)$, and, according to the second line in Eq. (17), in $\langle C''\rangle_{1/w}$ as well.

On the other hand, $\langle a\rangle_w$ and $A\langle a'\rangle_{1/w}$ essentially coincide once a exceeds the range where a is noticeable. Indeed, the main contributions to those averages come from the vicinity of $z = d$ where the integrands in Eqs. (16) and (17) (first line) match. Expanding $w(\zeta)$ about this turning point, one finds that $\langle a\rangle_w \sim A^{-1/2}$ whereas $\langle a'\rangle_{1/w} \sim A^{-3/2}$, just like

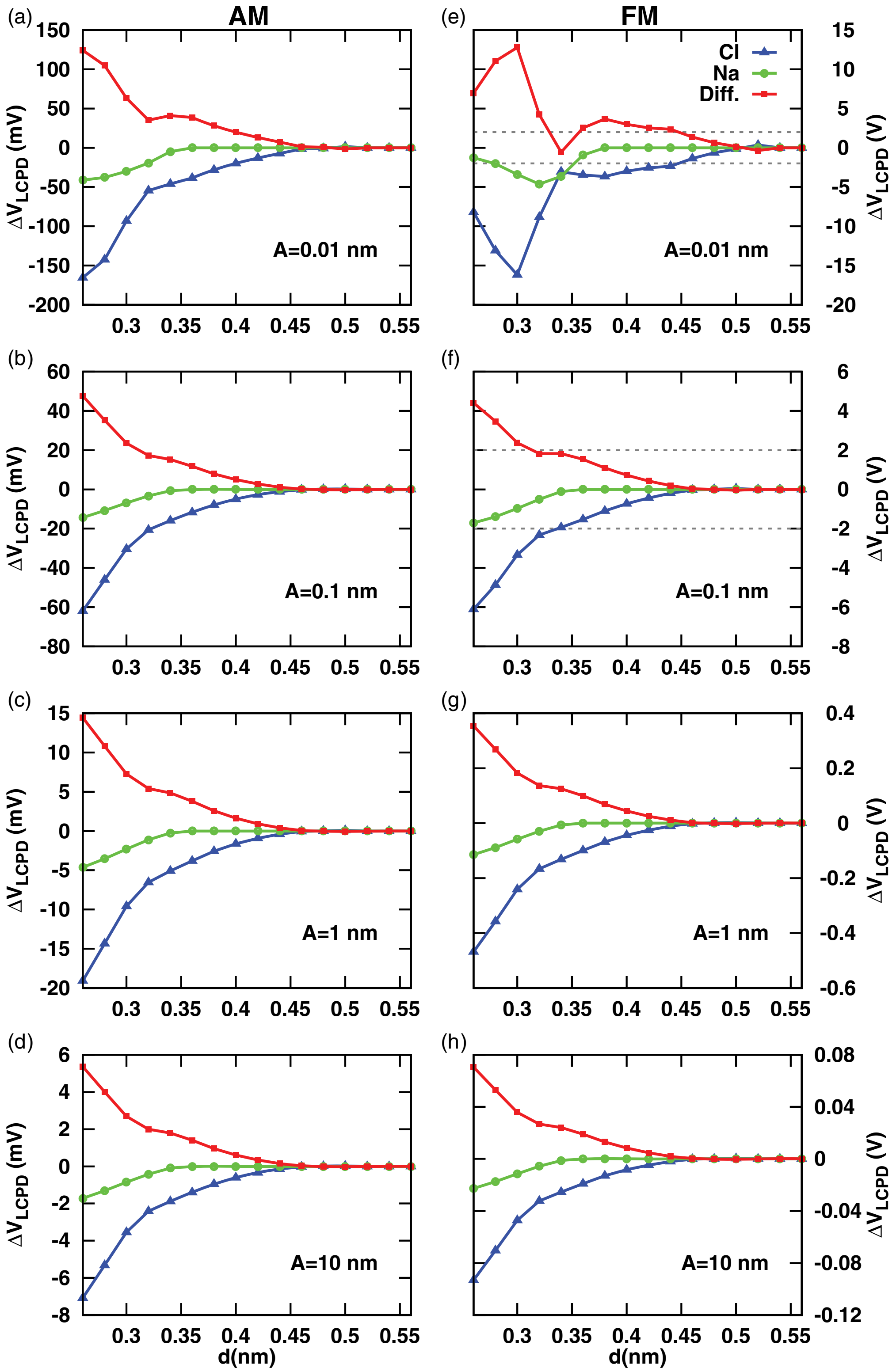

FIG. 12. (Color online) Calculated deviations ΔV_{LCPD} for AM- (left column) and FM-KPFM (right column) versus closest tip apex-sample distance for tip oscillation amplitudes $A = 0.01$ nm (a) and (e), $A = 0.1$ nm (b) and (f), $A = 1$ nm (c) and (g), and $A = 10$ nm (d) and (h). In (e) and (f), the dashed horizontal lines indicate the range of validity of our DFT calculations (±2 V).

Δf_1 behaves in NCAFM.[87] According to Figs. 11(b) and 11(c), the same argument cannot be applied to $\langle C'' \rangle_{1/w}$ for $A \leqslant 10$ nm, and not at all to $\langle C' \rangle_w$ because $C'(s)$ varies only slowly up to $s = R = 20$ nm. Figure 13 shows how the finite oscillation amplitude affects the relevant cycle averages as well as ΔV_{LCPD} in the AM mode (left column) and in the FM mode (right column) at the closest tip apex-sample separation $d = 0.30$ nm indicated by arrows in Fig. 9.

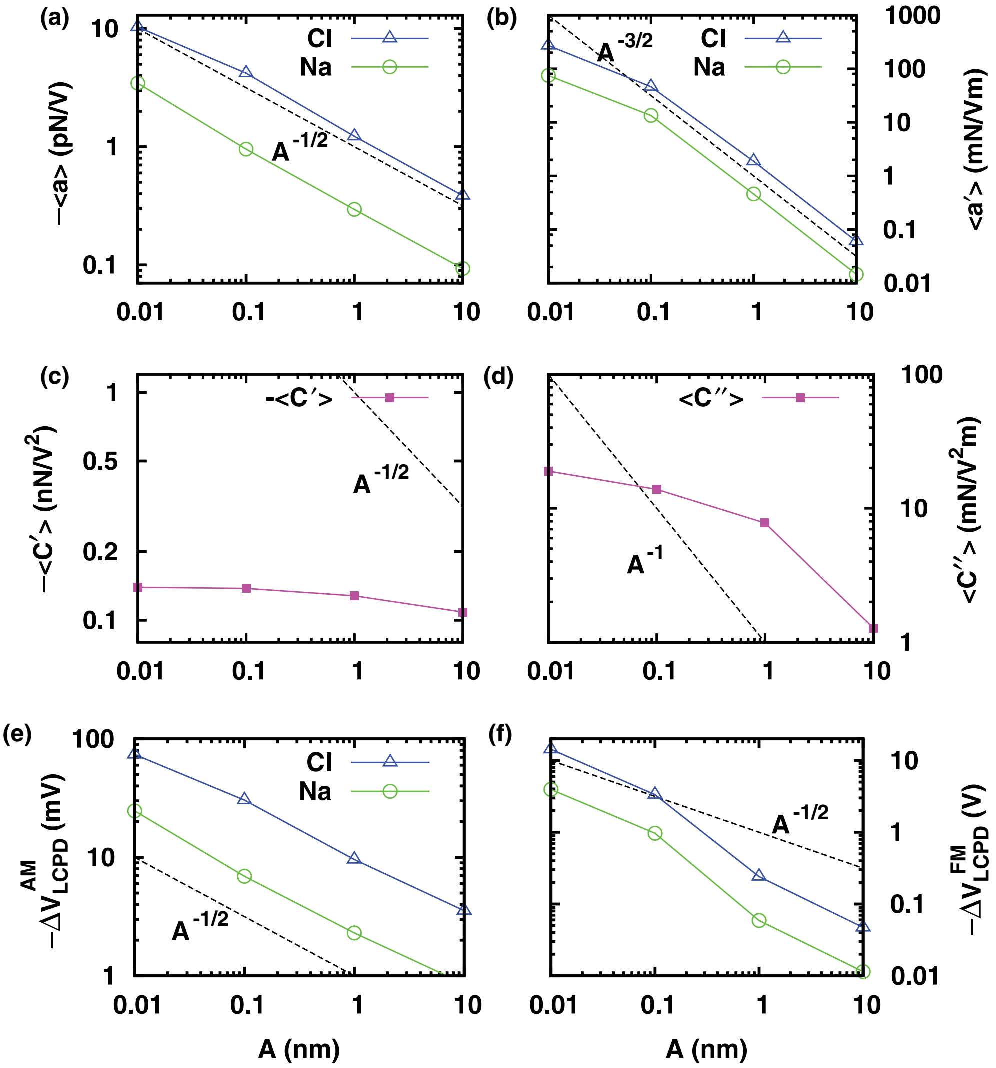

FIG. 13. (Color online) Amplitude dependencies of the cycle averages $\langle a\rangle_w$ and $\langle a'\rangle_{1/w}$ (a) and (b), $\langle C'\rangle_w$ and $\langle C''\rangle_{1/w}$ (c) and (d) and of the resulting deviations $\Delta V_{\mathrm{LCPD}}^{\mathrm{AM}}$ and $\Delta V_{\mathrm{LCPD}}^{\mathrm{FM}}$ (e) and (f) at a closest tip apex separation of $d = 0.3$ nm above Cl and Na surface sites.

The same trends persist at all separations $d < 0.5$ nm where LCPD contrast appears. $\langle a\rangle_w$ drops as $A^{-1/2}$, and $\langle a'\rangle_{1/w}$ drops as $A^{-3/2}$ already beyond $A = 0.1$ nm, while $\langle C'\rangle_w$ varies only little and $\langle C''\rangle_{1/w}$ begins to drop somewhat slower than A^{-1} only above $A = 1$ nm. The resulting amplitude dependencies in both modes reflect the different dependencies of the numerators and denominators in Eqs. (14) and (15).

D. Discussion and experimental limitations

Expressions formally similar to Eqs. (12) and (13) were obtained in Refs. 26, 28, and 47. However, their denominators came from a short-range polarization contribution $\propto V^2$ to the microscopic force F_μ rather than from the much larger capacitive force F_M. Nony *et al.*[47] also noticed that $\langle a\rangle_w$ and $A\langle a'\rangle_{1/w}$ almost coincide when A exceeds a few nanometers. This results in a comparable ΔV_{LCPD} for AM and FM modes if A exceeds a few nanometers. However, by including the correct F_M and taking into account the different amplitude dependencies of the denominators in Eqs. (14) and (15), we conclude that the contrast should remain larger in the FM than in the AM mode for a given closest approach distance d and oscillation amplitude A. This prediction is independent of the particular system considered, but the mode-dependent signal to noise ratio must also be considered. Thus Kawai *et al.*[35] calculated the minimum detectable CPD as a function of A and showed that it is smaller in the AM mode. Taking into account the discussions of Figs. 6 and 11, $\langle C'\rangle_w$ would be larger if the cantilever area is larger, whereas $\langle C''\rangle_{1/w}$ would be unaffected, whereas both quantities would be larger if the cone angle is broader or if the sample is a metal rather than an insulator, but $\langle C''\rangle_{1/w}$ would be more strongly affected. On the other hand, $\langle a\rangle_w$ and $\langle a'\rangle_{1/w}$ would be larger if the tip apex is charged[48] rather than neutral, or if the sample is a semiconductor with a reconstructed surface which exposes partially charged species like Si(111) 7 × 7.[18,35] From this point of view, the system studied here is especially challenging. Furthermore, the contrast ratio slowly decreases if A is increased, e.g., by a factor which drops from about 100 to 10 for oscillation amplitudes between 0.01 and 10 nm in our example.

For a meaningful comparison with NCAFM-KPFM measurements, it is important to take experimental limitations into account. In view of the long-range LCPD variations due to surface and bulk inhomogeneities on real samples, one should compare computed atomic-scale LCPD variations with the difference between the LCPD measured at subnanometer separations d in the middle of a flat homogeneous island or terrace and the extrapolated long-range, essentially site-independent LCPD. This procedure would also suppress most of the long-range contributions to $\langle a \rangle_w$ and $\langle a' \rangle_{1/w}$, which would arise in the case of a charged or strongly polar tip.[25] Moreover, the comparison should be done with the same tip at constant d (slow distance control) because atomic-scale variations of d at constant $\Delta f_1(x,y,d)$ would induce such variations in the LCPD even if the latter is site-independent but has a different distance dependence as Δf_1.

For the distance controller to function properly, Δf_1 must be chosen on the branch where this frequency shift becomes more negative if d is decreased. Furthermore, the maximum restoring force kA must be much larger than the maximum tip-sample attraction.[87] For measurements with standard NCAFM cantilevers ($k \sim 20$–40 N/m) this criterion is typically satisfied by using oscillation amplitudes $A > 5$ nm, and atomically resolved imaging is typically performed at distances $d \sim 0.4$–0.5 nm. According to Fig. 12, the LCPD contrast which is then predicted to be 20–100 mV in the FM mode and a few mV in the AM mode approaches the experimental limits in both modes. Even if the AM-KPFM signal is enhanced by setting the modulation frequency at the second flexural resonance of the cantilever, the LCPD contrast predicted by our model would remain the same. This contrast would be stronger if the tip were charged. Unfortunately, available data showing atomic-scale contrast on (001) surfaces of NaCl and KBr is insufficient for a meaningful comparison between AM and FM KPFM. However, LCPD maps obtained with sputter-cleaned Si tips and similar measurement parameters on Si(111) 7×7 surfaces show that the contrast between Si adatoms and corner holes in the FM-mode[18] is about ten times stronger than in the AM-mode.[35] Moreover, data obtained from a direct determination of the maximum of Δf_1 versus bias voltage V_b agreed well with those obtained by nulling the FM-KPFM signal at the modulation frequency.[18]

The sizable LCPD contrast of several Volts predicted in the FM mode for amplitudes $A < 0.1$ nm should, however, be readily observable when using a tuning fork instead of a cantilever. Owing to the much higher stiffness $k \simeq 1800$ N/m of this deflection sensor, the above-mentioned criterion can be satisfied with such amplitudes close to the ultrasmall limit.[11] Combined NCAFM-KPFM measurements using such tuning forks with PtIr tips have only been done at low temperature by the time-consuming direct method mentioned in Introduction.[19,20] Unfortunately, no FM-KPFM measurements showing atomic-scale LCPD contrast on alkali halide (001) surfaces have so far been reported.

V. SUMMARY AND OUTLOOK

We proposed a general multiscale approach to compute electrostatic forces responsible for atomic-scale contrast in KPFM performed simultaneously with NCAFM. Although attention is focused on insulating samples and results are presented for a silicon tip interacting with a NaCl(001) sample, the approach is not restricted to particular sample or tip materials. The problem is split into two parts coupled in a remarkably simple but novel fashion. First, the electrostatic problem of the voltage-biased AFM probe (including the tip and the cantilever) against the grounded sample, treated as macroscopic perfect conductors or insulators, is solved by a finite-difference method with controlled accuracy on a nonuniform mesh. The method is capable of treating complex geometries with widely different dimensions, but is illustrated here for systems with cylindrical symmetry. The solution yields the electric potential and field distributions and the capacitance $C(s)$ of the system from which the electrostatic force F_M acting on the probe and its gradient are calculated as functions of the macroscopic tip-sample separation s. By comparing results obtained with and without the cantilever as well as with the analytic solution for a tip approximated by a conducting sphere in Appendix B, the contributions of the cantilever, the conical tip shank and of its spherical end can be recognized. If the sample is a thick insulator, all three affect the macroscopic force, whereas the last two affect the force gradient even at sub-nanometer separations relevant for atomic-scale contrast.

Instead of the bias voltage V_b, the nearly uniform electric field obtained in that range is then applied as an external field to the microscopic part which can be treated by empirical atomistic or first principles methods. The *ab initio* BigDFT wavelet code employed here enables one to compute the short-range bias-dependent force on the tip apex represented by a cluster with an unprecedented accuracy of 1 pN. For the Si-nanotip-NaCl(001) system considered here, this microscopic force F_μ is a linear function of the bias in the investigated range $V_b - V_{\mathrm{CPD}} = \pm 2$ V. We argue that this is a general result, except close to atomic-scale instabilities caused by strong enough forces which could arise at very small separations and/or very large effective biases.

Adding the macroscopic and microscopic bias-dependent forces, expressions are obtained for the KPFM signals in the AM and the FM modes. The atomic-scale deviation ΔV_{LCPD} of the local CPD from its common value at large separations is the ratio of the derivatives $a = dF_\mu/dV_b$ and dC/ds averaged over the tip oscillation amplitude with different weights in AM- and FM-KPFM, as described by Eqs. (14) and (15). We explain the amplitude dependence of the atomic-scale LCPD contrast in both modes and predict that for typical amplitudes used in measurements with standard NCAFM cantilevers, this contrast should be much stronger in the FM mode. This is a consequence of the contributions of the cantilever and the tip shank to the KPFM signal in the AM mode, which are stronger on insulating samples. The same conclusion has previously been reached in comparisons of AM- and FM-KPFM measurements of long-range LCPD variations; such variations are caused by interactions of the biased probe with CPD inhomogeneities and surface charges on scales of several nanometers and above on conducting samples partly covered with ultrathin overlayers of different materials.[15,36] However, the strong mode-dependent influence of distant contributions to dC/ds on the atomic-scale LCPD contrast has, to our knowledge, not been recognized because previous work on this topic assumed that only the tip apex mattered at subnanometer separations.

Because ΔV_{LCPD} depends on measurement parameters, it is desirable to extract the more fundamental quantity $a = dF_\mu/dV_b$ from combined KPFM measurements, just like the microscopic force F_μ is extracted from NCAFM measurements using, e.g., a widely accepted inversion algorithm[69] or one based on the direct inversion of the discretized version of the first line of Eq. (15) described in Appendix A by back substitution.[88] Since ΔV_{LCPD} is predicted to be stronger in FM-KPFM, whereas its distance dependence is governed by the weighted average $\langle a' \rangle_{1/w}$ modes, the most appealing way to obtain $a(d)$ would be to extract a' then integrate it from the range where ΔV_{LCPD} vanishes down to the desired separation d. The averages $\langle a' \rangle_{1/w}$ and $\langle C'' \rangle_{1/w}$ can be separately obtained from direct measurements of the frequency shift Δf_1 as a function of bias,[18] namely, from the shift of the maximum and the curvature of parabolic fits at several (x,y,d) positions. The signal-to-noise ratio of those averages can be improved by using ac modulation and lock-in detection at the modulation frequency. The averages could then be determined from the zero intercept $V_{\mathrm{LCPD}}^{\mathrm{FM}}$ and the slope of the FM-KPFM signal $\langle \Delta f_\omega \rangle_w$ versus dc bias. An analogous procedure could be applied to determine $\langle a \rangle_w$ and $\langle C' \rangle_w$ from the AM-KPFM signal $\langle F_\omega \rangle_w$, then a itself by inversion, using suitably modified algorithms.[88,89] Because the AM-KPFM signal-to-ratio is much superior if the modulation frequency f is at the second cantilever resonance,[35] $\Delta V_{\mathrm{LCPD}}^{\mathrm{AM}}$ could be determined more accurately even if it is smaller than in FM-KPFM.

In any case, note that the slope a reflects variations of the electrostatic potential outside the sample surface which are, however, locally enhanced by the proximity of the tip apex. Since the latter is in turn also polarized and deformed,[90] a cannot simply be described as the convolution of the unperturbed electrostatic potential with a merely distance-dependent tip point-spread function, as in macroscopic electrostatics.[43]

Complications due to averaging over the tip oscillation amplitude are to a certain extent avoided with tuning fork deflection sensors which enable direct measurements of $\langle \Delta f_\omega \rangle_w$ versus bias, using amplitudes approaching the ultrasmall limit.[19,20] Spectacular results have thus been obtained on isolated molecules adsorbed on a thin epitaxial NaCl(001) film by using tips with well defined apex species stable at low temperature.[24] Most recently, $V_{\mathrm{LCPD}}^{\mathrm{FM}}$ contrast reflecting changes in the intramolecular charge distribution has been observed upon a configurational switch triggered by a judiciously applied pulse.[23] Our results shown in Figs. 12(e), 12(f), and 13(d) show that $\Delta V_{\mathrm{LCPD}}^{\mathrm{FM}}$ and a' still have a significant amplitude dependence between $A = 0.1$ and 0.01 nm, so that inversion is still necessary to obtain accurate results for typical amplitudes used with tuning fork sensors.

Since such measurements use hard metal tips, while metal-coated tips are also used in NCAFM and/or KPFM measurements with cantilevers it would desirable to develop appropriate nanotip models and to perform simulations like those described here. In particular, the recently fabricated sharp and stable W and Cr coated silicon tips[74,86] and the stable atomic-scale resolution achieved with Cr-coated cantilevers at separations exceeding the usual range $d < 0.5$ nm merit further attention. Atoms or molecules intentionally picked by the apex and/or adsorbed on the sample[20,23,24,27] would be worth studying using our approach in order to take into account modifications of their electronic and geometric structure due to bonding and charge transfer. Another class of systems which merit further investigations involve silicon nanotips with a picked-up cluster of foreign material, NaCl in particular, which have so far been studied by DFT in the absence of a sample[91] or represented by a cluster of the same material as the sample using empirical interaction potentials.[48,50]

Note finally that all macroscopic probe models, including ours, provide a better description of metallic or metal-coated tips than of real silicon tips. Indeed, even if the native oxide is removed by sputtering, a silicon layer of few nanometers depleted of charge carriers still separates the tip surface from the highly doped conducting tip interior. Although it was taken into account in previous treatments of KPFM of semiconductor devices[3], this depletion layer remains to be included when modeling Si tips, e.g., by allowing a smaller effective radius R of the equipotential at the applied bias voltage and a larger effective separation s from the sample surface.

ACKNOWLEDGMENTS

This work has been supported by the Swiss National Science Foundation (SNF) and the Swiss National Center of Competence in Research (NCCR) on Nanoscale Science. The CPU intensive computations were done at the Swiss National Supercomputing Center (CSCS) in Manno.

APPENDIX A: SIGN OF THE MACROSCOPIC ELECTROSTATIC FORCE

Using the virtual work method, the macroscopic electrostatic tip-sample interaction can be calculated from the potential energy stored in the capacitor formed between the tip and the back electrode. The (real) force acting on the tip F_z, which is considered constant during a virtual arbitrary infinitesimal tip displacement δz, performs a virtual work $\delta w = F_z\, \delta z = -\delta U$, where $U = U_c + U_b$ is the total energy of the system including contributions from both the capacitor and the biasing battery which maintains a fixed potential difference V between the electrodes. In response to this displacement, the battery transfers a charge δQ between the electrodes in order to keep their potential difference fixed. It costs a change of $\delta U_b = -\delta Q\, V$ in the energy of the battery. Whereas the energy of the capacitor changes by $\delta U_c = \frac{1}{2}\delta Q\, V$, which implies $U_b = -2U_c$, i.e.,

$$\delta U = \delta U_c + \delta U_b = -\delta U_c.$$

The electrostatic force is therefore

$$F_z = -\frac{\delta U}{\delta z} = +\frac{\delta U_c}{\delta z} = +\frac{1}{2}\frac{\delta C}{\delta z}V^2$$

and is always attractive because $\delta C/\delta z < 0$.

APPENDIX B: CONDUCTING SPHERE AGAINST A THICK DIELECTRIC SLAB

The force between a conducting sphere of radius R at potential V facing a dielectric slab grounded on the bottom can be calculated by means of the image charge method. For a semi-infinite dielectric, we found that the solution is given by remarkably simple generalization of the treatment in Sec. 5.08 of Smythe's textbook[64] for a semi-infinite conductor. Details, further analytic results, and useful approximations, which are of general interest for scanning force microscopy, will be presented elsewhere.[92] The potential Φ in the region between the sphere and the slab is generated by a series of point charges $\{q_n, z_n\}$ inside the sphere and their corresponding images $\{-\beta q_n, -z_n\}$ below the surface of the dielectric, where $\beta = (\epsilon - \epsilon_0)/(\epsilon + \epsilon_0)$, ϵ and ϵ_0 being the permittivities of the dielectric and of vacuum, respectively. The first charge $q_1 = 4\pi\epsilon_0 V R$ is located at the center of the sphere $z_1 = R + s$. Physically, the image charges represent the effect of the polarization induced at the surface of the dielectric which causes a jump discontinuity in E_z. Together with the other charges they ensure that the sphere surface remains equipotential at V.

We find

$$q_n = q_1 \sinh\alpha \left(\frac{\beta^{n-1}}{\sinh n\alpha}\right), \tag{B1}$$

where $\cosh\alpha = z_1/R$ and

$$z_n = R \sinh\alpha \coth n\alpha, \tag{B2}$$

as in Smythe's treatment ($\beta = 1$). Except at the contact point ($s = 0$), the charges q_n decay exponentially fast towards zero and this solution provides convenient expressions for the capacitance $C(s) = q_{\mathrm{sph}}/V$, where

$$q_{\mathrm{sph}} = \sum_{n=1}^{\infty} q_n = 4\pi\epsilon_0 R V \sinh\alpha \sum_{n=1}^{\infty} \frac{\beta^{n-1}}{\sinh n\alpha}, \tag{B3}$$

and the z component of the force $(dC/ds)V^2/2$

$$F_M = 2\pi\epsilon_0 V^2 \sum_{n=2}^{\infty} \frac{\beta^{n-1}}{\sinh n\alpha}(\coth\alpha - n\coth n\alpha), \tag{B4}$$

the force gradient dF_M/ds, and the electric field at $r = 0$, $z = 0$

$$E_z = \frac{V}{R}\frac{1+\beta}{\sinh\alpha} \sum_{n=1}^{\infty} \frac{\beta^{n-1}\sinh n\alpha}{\cosh^2 n\alpha}. \tag{B5}$$

These series have been used to evaluate the solid lines in Figs. 6 and 7. The truncation error can be reduced by generalizing a trick proposed for the conducting sphere-plane problem.[49] If a series is truncated at some $n = k$, the remainder can be summed up analytically if one assumes $z_{n>k} \simeq z_\infty = R\sinh\alpha$. Thus because $q_{n+1}/q_{n>k} \simeq \beta R/(z_1 + z_\infty)$,

$$q_\infty \equiv \sum_{n=k+1}^{\infty} q_n \simeq \frac{q_{k+1}}{1 - \beta R/(z_1 + z_\infty)} = \frac{q_{k+1}}{1 - \beta e^{-\alpha}}.$$

Adding the correction to the first five terms, q_{sph} is obtained with an accuracy of 10^{-5} for $\epsilon/\epsilon_0 = 5.9$, $s/R = 0.1$.

For an ideal conductor ($\beta = 1$), these expressions reduce to those of Smythe[64] and diverge in the limit $s \to 0$ (i.e., $\alpha \to 0$). In our case $\beta < 1$ and in the same limit, the resulting series converge and can, in fact, be summed explicitly.[92] The result for $F(s = 0)$ was given without proof in Eq. (2) of Ref. 57. For NaCl ($\epsilon/\epsilon_0 = 5.9$, $\beta = 0.71$), one obtains limiting values of $C/\pi\epsilon_0 R = 6.98$, $F/\pi\epsilon_0 V^2 = -6.77$ (i.e., $F = -0.188\ \mathrm{nN/V^2}$ independent of sphere radius), $F'/\pi\epsilon_0 V^2 R^{-1} = 188.7$ and $E/VR^{-1} = 20.4$. In the case of a dielectric slab of finite thickness t, mirror images of all previously mentioned charges with respect to the grounded back-electrode must also be considered. They ensure that the field lines inside the dielectric become perpendicular to the grounded back-electrode instead of spreading radially. If $z_1 = R + s \ll t$, further image charges induced by those mirror charges can be neglected to order $\mathcal{O}((z_1/t)^2)$. Moreover, the electric force exerted by the mirror charges on the biased sphere can then be approximated as the Coulomb force between q_{sph} at its center and a lumped mirror charge $-(1-\beta)q_{\mathrm{sph}}$, $2(z_1 + t)$ away, i.e.,

$$F_{\mathrm{add}} \simeq \frac{-(1-\beta)}{4\pi\epsilon_0}\frac{q_{\mathrm{sph}}^2}{(2t)^2} = \pi\epsilon_0 V^2 \frac{2\epsilon_0}{\epsilon + \epsilon_0}\left(\frac{R}{t}\right)^2 \left(\frac{q_{\mathrm{sph}}}{q_1}\right)^2.$$

For relevant values $s < R \sim 10$ nm and $t \sim 1$ mm, this correction is below $(R/t)^2/6.8 \sim 10^{-11}$ times the force given by Eq. (B4), i.e., negligible in practice. A similar expression of comparable magnitude was proposed in Ref. 47, but was erroneously assumed to represent F_M.

APPENDIX C: DISCRETIZED INTEGRALS FOR FINITE TIP OSCILLATION AMPLITUDES

Assuming that $N + 1$ equispaced data points $\{z_i\}$ are sufficiently close together such that $g(z)$ remains almost constant within an interval length $\delta = 2A/N$, the integration in Eq. (16) can be approximated by a finite sum:

$$\langle g(z)\rangle_w \simeq \frac{1}{\pi}\sum_{i=0}^{N} w_i g_i,$$

where $g_i \equiv g(z_i)$ is either $g_i = a(z_i)$ or $g_i = C(z_i + h)$. Since $w(\zeta) = 1/\sqrt{A^2 - \zeta^2}$, we obtain

$$w_i = \int_{\zeta_i^-}^{\zeta_i^+} w(\zeta)d\zeta = \arcsin\left(\frac{\zeta_i^+}{A}\right) - \arcsin\left(\frac{\zeta_i^-}{A}\right),$$

where $\zeta_i^\pm = (i \pm \frac{1}{2})\delta - A$ are the midpoints between ζ_i and $\zeta_{i\pm 1}$. Taking into account the rapid variation of $w(\zeta)$ near the integration limits defined as $\zeta_0^- = -A$ and $\zeta_N^+ = A$, the square-root singularities of $w(\zeta)$ at those turning points are approximately included with this modified trapezoid integration method. Sufficiently far from those points, $w_i \simeq w(\zeta_i)\delta$ so that the standard trapezoid approximation is recovered. The analogous approximation for Eq. (17), namely,

$$\langle g'(z)\rangle_{1/w} = \langle g(z)\rangle_{\zeta w} \simeq \frac{1}{\pi}\sum_{i=0}^{N} w_i^* g_i$$

involves[88]

$$w_i^* = \frac{1}{A}\int_{\zeta_i^-}^{\zeta_i^+} \zeta w(\zeta)d\zeta = \sqrt{1 - \left(\frac{\zeta_i^-}{A}\right)^2} - \sqrt{1 - \left(\frac{\zeta_i^+}{A}\right)^2}.$$

Note that in the $A \to 0$ limit, only the data points at the two limits are taken into account. Indeed, if $N = 1$, $A = \delta/2$, and $W_0 = W_1$, hence $\langle g\rangle_w = (g_0 + g_N)/2$, and $W_0^* = -W_1^*$, hence $\langle g'\rangle_{1/w} = (g_N - g_0)/2A$, so that Eqs. (14) and (15) consistently approximate the corresponding zero-amplitude equations, Eqs. (12) and (13). Similarly, if $N = 2$, $A = \delta$ and one obtains $w_0 = w_2, w_1 = 0$ and $w_0^* = -w_2^*, w_1^* = 0$ and Eqs. (12) and (13) are again recovered.

[1] J. Weaver and D. Abraham, J. Vac. Sci. Technol. B **9**, 1559 (1991).

[2] M. Nonnenmacher, M. O'Boyle, and H. Wickramasinghe, Appl. Phys. Lett. **58**, 2921 (1991).

[3] S. Sadewasser, T. Glatzel, M. Rusu, A. Jager-Waldau, and M. C. Lux-Steiner, Appl. Phys. Lett. **80**, 2979 (2002).

[4] C. Barth, A. S. Foster, C. R. Henry, and A. L. Shluger, Adv. Mater. **23**, 477 (2011).

[5] S. Sadewasser and T. Glatzel, *Kelvin Probe Force Microscopy: Measuring and Compensating Electrostatic Forces* (Springer, Heidelberg, Dordrecht, London, New York, 2011).

[6] L. D. Landau, E. M. Lifshitz, and L. P. Pitaevskii, *Electrodynamics of Continuous Media*, 2nd ed. (Pergamon, Oxford, 1993), Chap. 3.

[7] D. P. Woodruff and T. A. Denchar, *Modern Techniques of Surface Science*, 2nd ed. (Cambridge University Press, Oxford, 1994), Chap. 7.

[8] F. E. Olsson and M. Persson, Surf. Sci. **540**, 172 (2003).

[9] C. Barth and C. R. Henry, Phys. Rev. Lett. **98**, 136804 (2007).

[10] F. J. Giessibl, Science **267**, 68 (1995).

[11] F. J. Giessibl, Rev. Mod. Phys. **75**, 949 (2003).

[12] T. R. Albrecht, P. Grütter, D. Horne, and D. Rugar, J. App. Phys. **69**, 668 (1991).

[13] A. Kikukawa, S. Hosaka, and R. Imura, Rev. Sci. Instrum. **67**, 1463 (1996).

[14] S. Kitamura and M. Iwatsuki, Appl. Phys. Lett. **72**, 3154 (1998).

[15] U. Zerweck, C. Loppacher, T. Otto, S. Graftsröm, and L. M. Eng, Phys. Rev. B **71**, 125424 (2005).

[16] F. J. Giessibl, Appl. Phys. Lett.**73**, 3956 (1998).

[17] M. Guggisberg, M. Bammerlin, C. Loppacher, O. Pfeiffer, A. Abdurixit, V. Barwich, R. Bennewitz, A. Baratoff, E. Meyer, and H.-J. Güntherodt, Phys. Rev. B **61**, 11151 (2000).

[18] S. Sadewasser, P. Jelinek, C.-K. Fang, O. Custance, Y. Yamada, Y. Sugimoto, M. Abe, and S. Morita, Phys. Rev. Lett. **103**, 266103 (2009).

[19] T. König, G. H. Simon, H.-P. Rust, and M. Heyde, J. Phys. Chem. C **113**, 11301 (2009).

[20] L. Gross, F. Mohn, P. Liljeroth, J. Repp, F. J. Giessibl, and G. Meyer, Science **324**, 1428 (2009).

[21] H. Diesinger, D. Deresnes, J. Nys, and T. Mélin, Ultramicroscopy **108**, 773 (2008).

[22] C. Sommerhalter, T. W. Matthes, T. Glatzel, A. Jäger-Waldau, and M. C. Lux-Steiner, App. Phys. Lett. **75**, 286 (1999).

[23] F. Mohn, L. Gross, N. Moll, and G. Meyer, Nat. Nanotechnology **7**, 227 (2012).

[24] L. Gross, F. Mohn, N. Moll, P. Liljeroth, and G. Meyer, Science **325**, 1110 (2009).

[25] C. Barth, T. Hynninen, M. Bieletzki, C. R. Henry, A. S. Foster, F. Esch, and U. Heiz, New J. Phys. **12**, 093024 (2010).

[26] A. Masago, M. Tsukada, and M. Shimizu, Phys. Rev. B **82**, 195433 (2010).

[27] F. Bocquet, L. Nony, and C. Loppacher, Phys. Rev. B **83**, 035411 (2011) .

[28] M. Tsukada, A. Masago, and M. Shimizu, J. Phys.: Condens. Matter **24**, 084002 (2012).

[29] S. Kitamura, K. Suzuki, M. Iwatsuki, and C. Mooney, Appl. Surf. Sci. **157**, 222 (2000).

[30] K. Okamoto, Y. Sugawara, and S. Morita, Appl. Surf. Sci. **188**, 381 (2002).

[31] K. Okamoto, K. Yoshimoto, Y. Sugawara, and S. Morita, Appl. Surf. Sci. **210**, 128 (2003).

[32] F. Krok, K. Sajewicz, J. Konior, M. Goryl, P. Platkowski, and M. Szymonski, Phys. Rev. B **77**, 235427 (2008).

[33] G. H. Enevoldsen, T. Glatzel, M. C. Christensen, J. V. Lauritsen, and F. Besenbacher, Phys. Rev. Lett. **100**, 236104 (2008).

[34] F. Bocquet, L. Nony, C. Loppacher, and T. Glatzel, Phys. Rev. B **78**, 035410 (2008).

[35] S. Kawai, T. Glatzel, H.-J. Hug, and E. Meyer, Nanotechnology **21**, 245704 (2010).

[36] T. Glatzel, S. Sadewasser, and M. Lux-Steiner, Appl. Surf. Sci. **210**, 84 (2003).

[37] T. Glatzel, L. Zimmerli, S. Koch, B. Such, S. Kawai, and E. Meyer, Nanotechnology **20**, 264016 (2009).

[38] T. Hochwitz, A. K. Henning, C. Levey, C. Daghlian, and J. Slinkman, J. Vac. Sci. Technol. B **14**, 457 (1996).

[39] H. O. Jacobs, P. Leuchtmann, O. J. Homan, and A. Stemmer, J. Appl. Phys. **84**, 1168 (1998).

[40] S. Belaidi, F. Lebon, P. Girard, G. Leveque, and S. Pagano, Appl. Phys. A **66**, S239 (1998).

[41] J. Colchero, A. Gil, and A. M. Baró, Phys. Rev. B **64**, 245403 (2001).

[42] S. Gómez-Moñivas, L. S. Froufe, R. Carminati, J. J. Greffet, and J. J. Sáenz, Nanotechnology **12**, 496 (2001).

[43] E. Strassburg, A. Boag, and Y. Rosenwaks, Rev. Sci. Instrum. **76**, 083705 (2005).

[44] J. Konior, J. Appl. Phys. **101**, 084907 (2007).

[45] Y. Shen, D. M. Barnett, and P. M. Pinsky, Rev. Sci. Instrum. **79**, 023711 (2008).

[46] R. Baier, C. Leendertz, M. C. Lux-Steiner, and S. Sadewasser, Phys. Rev. B **85**, 165436 (2012).

[47] L. Nony, F. Bocquet, C. Loppacher, and T. Glatzel, Nanotechnology **20**, 264014 (2009).

[48] L. Nony, A. S. Foster, F. Bocquet, and C. Loppacher, Phys. Rev. Lett. **103**, 036802 (2009).

[49] L. Kantorovich, A. Foster, A. Shluger, and A. Stoneham, Surf. Sci. **445**, 283 (2000).

[50] R. Hoffmann, L. N. Kantorovich, A. Baratoff, H. J. Hug, and H.-J. Güntherodt, Phys. Rev. Lett. **92**, 146103 (2004).

[51] K. Ruschmeier, A. Schirmeisen, and R. Hoffmann, Phys. Rev. Lett. **101**, 156102 (2008).

[52] L. N. Kantorovich, A. I. Livshits, and M. Stoneham, J. Phys.: Condens. Matter **12**, 795 (2000).

[53] S. Hudlet, M. Saint Jean, C. Guthmann, and J. Berger, Eur. Phys. J. B **2**, 5 (1998).

[54] Y. Shen, D. M. Barnett, and P. M. Pinsky, Eng. Anal. Bound. Elem. **32**, 682 (2008).

[55] J. D. Jackson, *Classical Electrodynamics* (Wiley, New York, 2001).

[56] S. Belaidi, P. Girard, and G. Leveque, J. Appl. Phys. **81**, 1023 (1997).

[57] S. Gómez-Moñivas, L. S. Froufe-Pérez, A. J. Caamaño, and J. J. Sáenz, App. Phys. Lett. **79**, 4048 (2001).

[58] G. M. Sacha, E. Sahagún, and J. J. Sáenz, J. Appl. Phys. **101**, 024310 (2007).

[59] G. M. Sacha and J. J. Sáenz, Appl. Phys. Lett. **85**, 2610 (2004).

[60] G. Elias, T. Glatzel, E. Meyer, A. Schwarzman, A. Boag, and Y. Rosenwaks, Beilstein J. Nanotechnol. **2**, 252 (2011)

[61] S. Sadewasser, T. Glatzel, R. Shikler, Y. Rosenwaks, and M. Lux-Steiner, Appl. Surf. Sci. **210**, 32 (2003).

[62] G. Valdrè and D. Moro, Nanotechnology **19**, 405502 (2008).

[63] D. S. H. Charrier, M. Kemerink, B. E. Smalbrugge, T. de Vries, and R. A. J. Janssen, ACS Nano **2**, 622 (2008).

[64] W. R. Smythe, *Static and Dynamic Electricity*, 2nd ed. (McGraw-Hill, New York, 1950), Chap. 5.

[65] O. Schenk, M. Bollhöfer, and R. A. Römer, SIAM Review **50**, 91 (2008).

[66] O. Schenk, A. Wächter, and M. Hagemann, Comput. Optim. Appl. **36**, 321 (2007).

[67] http://pages.unibas.ch/comphys/comphys/software.

[68] U. Dürig, Appl. Phys. Lett. **75**, 433 (1999).

[69] J. E. Sader and S. P. Jarvis, Appl. Phys. Lett. **84**, 1801 (2004).

[70] T. Arai and M. Tomitori, Phys. Rev. Lett. **93**, 256101 (2004).

[71] T. Arai and M. Tomitori, Phys. Rev. B **73**, 073307 (2006).

[72] M. A. Lantz, H. J. Hug, R. Hoffmann, P. J. A. van Schendel, P. Kappenberger, S. Martin, A. Baratoff, and H.-J. Güntherodt, Science **291**, 2580 (2001).

[73] Y. Sugimoto, Y. Nakajima, D. Sawada, K. I. Morita, M. Abe, and S. Morita, Phys. Rev. B **81**, 245322 (2010).

[74] Y. Kinoshita, Y. Naitoh, Y. J. Li, and Y. Sugawara, Rev. Sci. Instr. **82**, 113707 (2011).

[75] M. Guggisberg, M. Bammerlin, A. Baratoff, R. Lthi, C. Loppacher, F. Battiston, J. L, R. Bennewitz, E. Meyer, and H.-J. Gntherodt, Surf. Sci. **461**, 255 (2000).

[76] A. J. Weymouth, T. Wutscher, J. Welker, T. Hofmann, and F. J. Giessibl, Phys. Rev. Lett. **106**, 226801 (2011).

[77] F. W. de Wette, W. Kress, and U. Schröder, Phys. Rev. B **32**, 4143 (1985).

[78] R. Bennewitz, A. S. Foster, L. N. Kantorovich, M. Bammerlin, C. Loppacher, S. Schär, M. Guggisberg, E. Meyer, and A. L. Shluger, Phys. Rev. B **62**, 2074 (2000).

[79] R. Bennewitz, A. S. Foster, L. N. Kantorovich, M. Bammerlin, C. Loppacher, S. Schär, M. Guggisberg, E. Meyer, and A. L. Shluger, Phys. Rev. B **62**, 2074 (2000).

[80] C. Hartwigsen, S. Goedecker, and J. Hutter, Phys. Rev. B **58**, 3641 (1998).

[81] L. Genovese, A. Neelov, S. Goedecker, T. Deutsch, S. A. Ghasemi, A. Willand, D. Caliste, O. Zilberberg, M. Rayson, A. Bergman, and R. Schneider, J. Chem. Phys. **129**, 014109 (2008).

[82] L. Genovese, T. Deutsch, A. Neelov, S. Goedecker, and G. Beylkin, J. Chem. Phys. **125**, 074105 (2006).

[83] S. Goedecker, J. Chem. Phys. **120**, 9911 (2004).

[84] S. A. Ghasemi, S. Goedecker, A. Baratoff, T. Lenosky, E. Meyer, and H. J. Hug, Phys. Rev. Lett. **100**, 236106 (2008).

[85] A. Sadeghi, A. Baratoff, and S. Goedecker (unpublished.)

[86] G. Teobaldi, K. Lämmle, T. Trevethan, M. Watkins, A. Schwarz, R. Wiesendanger, and A. L. Shluger, Phys. Rev. Lett. **106**, 216102 (2011).

[87] F. J. Giessibl, Phys. Rev. B **56**, 16010 (1997).

[88] O. Pfeiffer, Ph.D. thesis, Basel University, Basel, Switzerland, 2004.

[89] J. E. Sader and Y. Sugimoto, Appl. Phys. Lett. **97**, 043502 (2010).

[90] S. Kawai, T. Glatzel, S. Koch, A. Baratoff, and E. Meyer, Phys. Rev. B **83**, 035421 (2011).

[91] M. Amsler, S. A. Ghasemi, S. Goedecker, A. Neelov, and L. Genovese, Nanotechnology **20**, 445301 (2009).

[92] A. Sadeghi, A. Baratoff, and S. Goedecker (unpublished).